Reconciling the conflicting extent of overriding plate deformation before and during megathrust earthquakes in South America, Sunda, and northeast Japan

Mario D'Acquisto[1], Taco Broerse[1], Celine P. Marsman[1], Rob Govers[1]

[1]Tectonophysics Group, Department of Earth Sciences, Utrecht University, Netherlands

Corresponding author: Mario D'Acquisto (m.dacquisto@uu.nl)

Mario D'Acquisto (ORCID https://orcid.org/0000-0001-6321-1954)
Taco Broerse (ORCID https://orcid.org/0000-0002-3235-0844)
Celine P. Marsman (ORCID https://orcid.org/0000-0001-5691-6753)
Rob Govers (ORCID https://orcid.org/0000-0001-7148-8857)

Key Points:

- Interseismic overriding plate deformation along the Peru-Chile, Sunda and Japan trenches occurs mostly within 500-1000 km of the trench.
- Coseismic deformation occurs in a much wider region.
- 3D earthquake cycle models support our hypothesis that these observations result from a mechanical contrast in the overriding plates.

Abstract

We aim to better understand the overriding plate deformation during the megathrust earthquake cycle. We estimate the spatial patterns of interseismic GNSS velocities in South America, Southeast Asia, and northern Japan and the associated uncertainties due to data gaps and velocity uncertainties. The interseismic velocities with respect to the overriding plate generally decrease with distance from the trench with a steep gradient up to a "hurdle", beyond which the gradient is distinctly lower and velocities are small. The hurdle is located 500–1000 km away from the trench, for the trench-perpendicular velocity component, and either at the same distance or closer for the trench-parallel component. Significant coseismic displacements were observed beyond these hurdles during the 2010 Maule, 2004 Sumatra-Andaman, and 2011 Tohoku earthquakes. We hypothesize that both the interseismic hurdle and the coseismic response result from a mechanical contrast in the overriding plate. We test our hypothesis using physically consistent, generic, three-dimensional finite element models of the earthquake cycle. Our models show a response similar to the interseismic and coseismic observations for a compliant near-trench overriding plate and an at least 5 times stiffer overriding plate beyond the contrast. The model results suggest that hurdles are more prominently expressed in observations near strongly locked megathrusts. Previous studies inferred major tectonic or geological boundaries and seismological contrasts located close to the observed hurdles in the studied overriding plates. The compliance contrast probably results from thermal, compositional and thickness contrasts and might cause the observed focusing of smaller-scale deformation like backthrusting.

Plain Language Summary

The contact area between an oceanic plate that sinks into the Earth's mantle and a continental plate is commonly locked by friction, except during earthquakes. GPS observations give us a snapshot of the resulting deformation of the continental plate during the long period (decades to centuries) leading up to large earthquakes. We analyze available observations in South America, Southeast Asia, and northern Japan. We find evidence that suggests that these regions have substantial mechanical contrasts at variable distances from the plate boundary, without affecting the earthquake cycle. The contrasts approximately coincide with boundaries of tectonic blocks. Three-dimensional mechanical models indicate that a mechanical contrast may explain the

observations. Our expectation that the time interval between major earthquakes, or their size, are affected by the location of the contrast is not supported by the models.

1 Introduction

The great megathrust earthquakes of the previous decades happened while continuous geodetic networks were being deployed. After these earthquakes, many studies focused on constraining the coseismic fault slip by combining geodetic with seismological observations (e.g., Simons et al., 2011; Vigny et al., 2011). Postseismic processes like relocking, afterslip and viscoelastic flow started to become apparent in the geodetic measurements shortly after these events and continue today, spawning a rich variety of studies that cast new light on processes and rheological properties.

The first earthquake during the period of modern geodesy that revealed the widespread extent of coseismic deformation was the M_w 9.2 2004 Sumatra-Andaman earthquake. Remarkably, coseismic displacements were recorded at GNSS stations up to more than 3,000 km away from the megathrust (Vigny et al., 2005). Similarly, in 2010, GNSS stations up to 1,700 km from the trench, far into the South American continent, recorded displacement due to the M_w 8.8 Maule (Chile) earthquake (Pollitz et al., 2010). Likewise, Wang et al., 2011 observed significant coseismic static offsets up to 2,500 km away from the epicenter following the M_w 9.0 2011 Tohoku earthquake.

Strain that has accumulated during interseismic periods (mostly) recovers coseismically as well as postseismically, after all interseismic slip deficit has been released by large earthquakes. Studies that compare coseismic deformation to interseismic deformation have mostly focused on correlating the megathrust locking pattern to the coseismic slip pattern (e.g., Loveless and Meade, 2011; Moreno et al., 2010; Nocquet et al., 2017). Generally, observed interseismic velocities (relative to a stable overriding plate reference) are directed landward and decrease with distance from the trench. However, compared to the large extent of deformation due to the largest megathrust earthquakes, interseismic strain buildup seems to focus much closer to the margin of the overriding plate, within several hundreds of kilometers from the trench (e.g. Drewes and Heidbach, 2012; Kreemer et al., 2014; McKenzie and Furlong, 2021; Simons et al., 2007). In many locations where the full interseismic velocity profile with distance from the trench can be observed, a distinct break in the slope of the interseismic velocity gradient is observed; from a high velocity gradient near the trench to a small velocity gradient farther away (Brooks et al., 2003a; Khazaradze

and Klotz, 2003; McFarland et al., 2017a; Nocquet et al., 2014a). This observation fits well to the popular notion of separability of geodetic velocities due to either rotation of a rigid plate, as well as plate interactions in finite areas along plate margins (e.g. Altamimi et al., 2012; Kreemer et al., 2014).

The decrease in interseismic velocities, as a function of trench distance, can often be reproduced by locking of (a part of) the megathrust fault (modelled by backslip) in an elastic halfspace (Chlieh et al., 2008a; Liu et al., 2010a; Métois et al., 2012a; Ruegg et al., 2009a). For parts of the South American plate, Norabuena et al. (1998) were the first to point out interseismic strain accumulation further inland that is higher than could be explained by megathrust locking alone. In the latter and in subsequent studies on the Central Andes (Bevis et al., 2001; Brooks et al., 2003a; McFarland et al., 2017a; Norabuena et al., 1998; Shi et al., 2020) a seismically active backthrust is adopted to explain the observed interseismic strain accumulation up to the backthrust, and a stable interior beyond that. In other cases, a somewhat looser definition of decoupling of the near-trench region from the rest of the plate is used by defining slivers that allow for a wholesale rotation with respect to the remainder of the overring plate (Métois et al., 2014a; Nocquet et al., 2014a). Both explanations rely on faults or shear zones that decouple the base of the lithosphere up to some depth, often interpreted as deep, active backthrusts of ~200 km wide (McFarland et al., 2017a; Weiss et al., 2016a).

Interpretations of interseismic strain accumulation are commonly based on fully elastic models. Overriding plate velocities decrease rapidly with distance from the trench in these models. Postseismic stress relaxation demonstrates however that the mantle wedge and sub-slab asthenosphere behave viscoelastically. Models with a viscoelastic upper mantle predict interseismic velocities that decrease more slowly with distance from the trench (Wang et al., 2012). Higher viscosities result in more elastic-like behavior with strain accumulation that is more concentrated in the near-trench region (Li et al., 2020, 2015; Shi et al., 2020; Trubienko et al., 2013). Lower model viscosities result in interseismic velocities that remain significant up to thousands of kilometers into the overriding plate. To match the observed interseismic velocities with their viscoelastic models, Trubienko et al. (2013) and Li et al. (2015) use long-term (Maxwell) viscosities effectively in the range of $4.0–5.1 \cdot 10^{19}$ Pa·s when accounting for the use of plane-strain 2D models on the relaxation timescale (Melosh and Raefsky, 1983). However, these viscosities

are beyond the high end of the range of estimates of asthenospheric wedge viscosities ($4.0–10 \cdot 10^{18}$ Pa·s) from recent studies of postseismic viscous relaxation (see Section 4.9).

The South American margin has played a significant role in the development of ideas about interseismic strain accumulation because of the presence of a continuous region not interrupted by sea parallel to the margin. There are several other subduction zones with a continental overriding plate where the gradient of interseismic velocities is observable over a wide distance. Landward velocities in northern Honshu (Japan) and Hokkaido, recorded by GEONET before the 2003 Tokachi and 2011 Tohoku earthquakes (Sagiya et al., 2000a), show a fast decrease with trench distance. Likewise, interseismic velocities on Sumatra and Sunda before the 2004 earthquake show a decrease with distance from the trench (Prawirodirdjo et al., 1997; Simons et al., 2007a), even though the trench-parallel motions are strongly affected by the Sumatran Fault (Genrich et al., 2000a). More significant complications to observe the interseismic velocity gradient arise in other subduction margins like Cascadia, where other tectonic processes overprint the interseismic locking signal, like the Mendocino Crustal Conveyor (Furlong and Govers, 1999) and the northward migration of the Sierra Nevada-Great Valley block (Williams et al., 2006). In southern Honshu and Shikoku strain rates due to convergence on the Japan trench and Nankai trench are superimposed, which makes it difficult to isolate the far-field interseismic velocity pattern. As discussed in Govers et al. (2018), continental Alaska shows continuing postseismic relaxation following the 1964 Prince William Sound earthquake. For these reasons, we focus on margins with only moderate tectonic complexity: South America, Sunda, and the Japan Trench.

In the present study we address the apparently contrasting geodetic observation that interseismic deformation of the overriding plate focusses within several hundreds of kilometers from the trench, whereas coseismic strain release extends over much greater distances. We observe a break in the slope of trench-parallel and trench-perpendicular velocity components as a function of trench distance, which we refer to as a hurdle. Long-lived subduction tectonically accretes blocks and rejuvenates the overriding plate, by an amount that is preconditioned by lithospheric strength contrasts (Mouthereau et al., 2013; Pearson et al., 2013). These strength contrasts remain visible today as significant contrasts in the effective elastic thickness of the lithosphere (Watts, 2015) that correlate with tectonic boundaries between blocks of vastly different ages (Stewart and Watts, 1997; Watts et al., 1995). Convergent deformation, including backthrusts, likely localizes at these naturally occurring contrasts. Here we consider the possibility that these lateral contrasts cause the

hurdle-like behavior of the overring plate. Because of our context of the earthquake cycle we consider contrasts in elastic properties.

Our study consists of two main elements: mapping the patterns of interseismic velocities and secondly the interpretation of interseismic velocity gradients in terms of mechanical contrasts. We characterize the spatial pattern of horizontal interseismic surface motion along the South America Trench, the Sunda Trench and Japan Trench based on available observations (Section 2). Near-trench regions are typically (much) more densely instrumented than intermediate and far-field regions, and interseismic velocities of benchmarks have variable uncertainties. We pay particular attention to assessing how these factors propagate into uncertainties in the interpolated velocity fields. We estimate the approximate location of the hurdle, the dominant break in the slope of interseismic velocities, and discuss its significance.

To test our hypothesis that hurdle-like behavior is related to elastic contrasts in the overriding plate, we construct a three-dimensional viscoelastic numerical model (Section 3), analyze our model results and their robustness (Section 4). Next we discuss their significance and possible interpretations in the context of other proposed causes (Section 5). We conclude (Section 6) that a mechanical contrast in the overriding plate, with a weaker near-trench region and a stronger far-field region, is a likely candidate for explaining both the interseismic and coseismic observations in the three analyzed subduction zones.

2 Analysis of interseismic velocity observations

2.1 Data selection

We compile previously published horizontal velocities along three convergent margins with abundant GNSS observations from interseismic periods: the Peru-Chile Trench (South America) (Alvarado et al., 2014a; Blewitt et al., 2016a; Brooks et al., 2011a, 2003a; Chlieh et al., 2004a; Drewes and Heidbach, 2012a; Gagnon et al., 2005a; Kendrick et al., 2001a; Klein et al., 2018a; Klotz et al., 2001a; McFarland et al., 2017a; Métois et al., 2014a, 2013a, 2012a; Nocquet et al., 2014a, 2014a; Ruegg et al., 2009a; Seemüller et al., 2010a; Weiss et al., 2016a), the Sunda Trench (Sumatra and Java, Indonesia) (Bock et al., 2003a; Chlieh et al., 2008a; Genrich et al., 2000a; Koulali et al., 2017a; Kreemer et al., 2014a; Prawirodirdjo et al., 2010a; Simons et al., 2007a), and

the Japan Trench (Apel et al., 2006a; Freed et al., 2017; Jin and Park, 2006a; Kreemer et al., 2014a; Liu et al., 2010a; Nishimura, 2011a; Ohzono et al., 2011a; Sagiya et al., 2000a; Shestakov et al., 2011a; Yoshioka, 2013a). To prevent contamination by postseismic transient signals, we exclude velocities computed using postseismic observations in the trench-perpendicular sector of the overriding plate where significant ($M_w \geq 7.5$) earthquakes affected the observations (see Figure 1). We use velocities expressed in the global reference frame ITRF (Altamimi et al., 2011). For the majority of our data sources we make use of the velocity tables from Kreemer et al. (2014), who have estimated a translation rate and rotation rate for each published set of velocities to express velocities in the same IGS08 reference frame (the IGS realization of ITRF). We feature velocities expressed in ITRF2005, ITRF2008 as well as ITRF2014; differences resulting from these different realizations are well below the 1 mm/yr level (Métivier et al., 2020). We also include velocities from Weiss et al. (2016), which are only provided in a self-determined, non-explicit South America reference frame. However, biases because of different reference frames are small, the mean difference in velocities between those of Weiss and the South America far-field velocities of Blewitt et al., 2016) is below 0.2 mm/yr.

Subsequently, we transform ITRF-expressed velocities to the overriding plate reference. For the sites in South America and Japan we apply the South America and Okhotsk Euler poles, respectively, of Kreemer et al. (2014). For Sumatra we make use of the Sunda Euler pole of Simons et al. (2007), who identify Sundaland as a coherent block moving independently of the South China block farther north. More information about data sources is available in Text S1 and Tables S1, S2 and S3. The resulting interseismic velocities, described in a consistent reference frame throughout each studied region, show a clear contrast between high near-trench velocities and a stable interior (Figure 1).

2.2 Velocity decomposition into trench-perpendicular and -parallel components

Along many subduction zones, the deformation due to oblique interplate convergence is partitioned into distinct trench-perpendicular and trench-parallel fault slip and strain (Fitch, 1972; McCaffrey, 1996, 1992). Strain partitioning not only implies that margin-parallel shear is accommodated on different faults than the convergent motion, but also that margin-parallel and margin-perpendicular interseismic deformation may be distributed differently in the overriding

plate. Using straight lines from the trench to identify margin-perpendicular and -parallel directions at each observation point can lead to sharp contrasts in each direction between nearby observation locations, depending on the trench geometry, and produces ambiguity in the case of a convex plate margin. Therefore, we define a conformal (i.e., angle-preserving) projection, specifically a Schwarz-Christoffel map (Driscoll, 2002), to identify trench-perpendicular and -parallel directions throughout each of the three study areas. This leads to a coordinate system that is locally trench-perpendicular at the trench, and that smoothly grades into a regional/plate-wide trench-perpendicular orientation with increasing distance from the trench. The derivatives in transformed coordinates express the angles between the local east and north-directions and the local trench-perpendicular and -parallel directions, allowing us to compute the relevant, orthogonal, trench-perpendicular and trench-parallel components of each velocity vector at any location, see Figure 1.

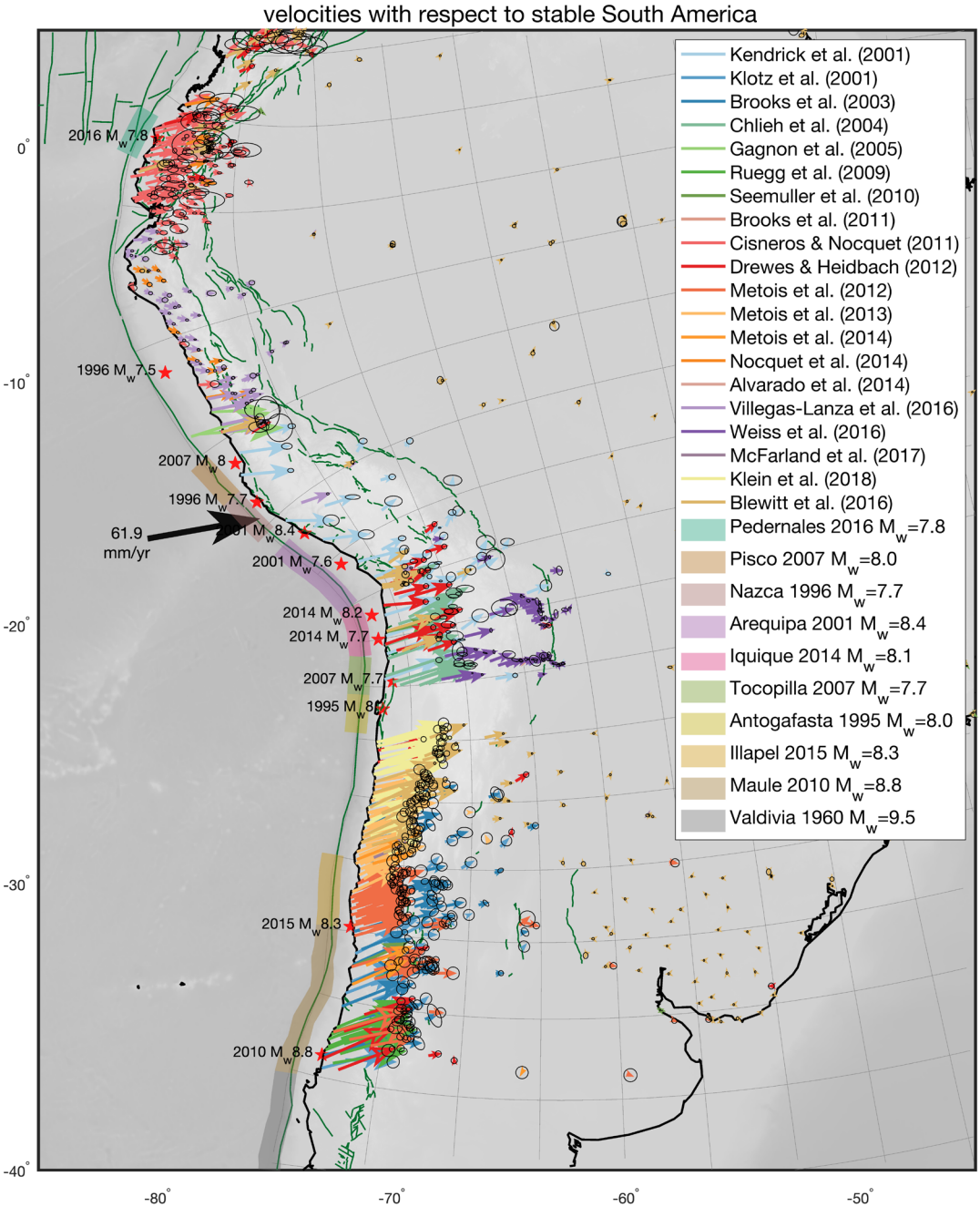
velocities with respect to stable South America
Kendrick et al. (2001)
Klotz et al. (2001)
Brooks et al. (2003)
Chlieh et al. (2004)
Gagnon et al. (2005)
Ruegg et al. (2009)
Seemuller et al. (2010)
Brooks et al. (2011)
Cisneros & Nocquet (2011)
Drewes & Heidbach (2012)
Metois et al. (2012)
Metois et al. (2013)
Metois et al. (2014)
Nocquet et al. (2014)
Alvarado et al. (2014)
Villegas-Lanza et al. (2016)
Weiss et al. (2016)
McFarland et al. (2017)
Klein et al. (2018)
Blewitt et al. (2016)
Pedernales 2016 Mw=7.8
Pisco 2007 Mw=8.0
Nazca 1996 Mw=7.7
Arequipa 2001 Mw=8.4
Iquique 2014 Mw=8.1
Tocopilla 2007 Mw=7.7
Antogafasta 1995 Mw=8.0
Illapel 2015 Mw=8.3
Maule 2010 Mw=8.8
Valdivia 1960 Mw=9.5
2016 Mw 7.8
1996 Mw 7.5
2007 Mw 8
1996 Mw 7.7
2001 Mw 8.4
2001 Mw 7.6
2014 Mw 8.2
2014 Mw 7.7
2007 Mw 7.7
1995 Mw 8
2015 Mw 8.3
2010 Mw 8.8
61.9
mm/yr
0°
-10°
-20°
-30°
-40°
-80°
-70°
-60°
-50°

209

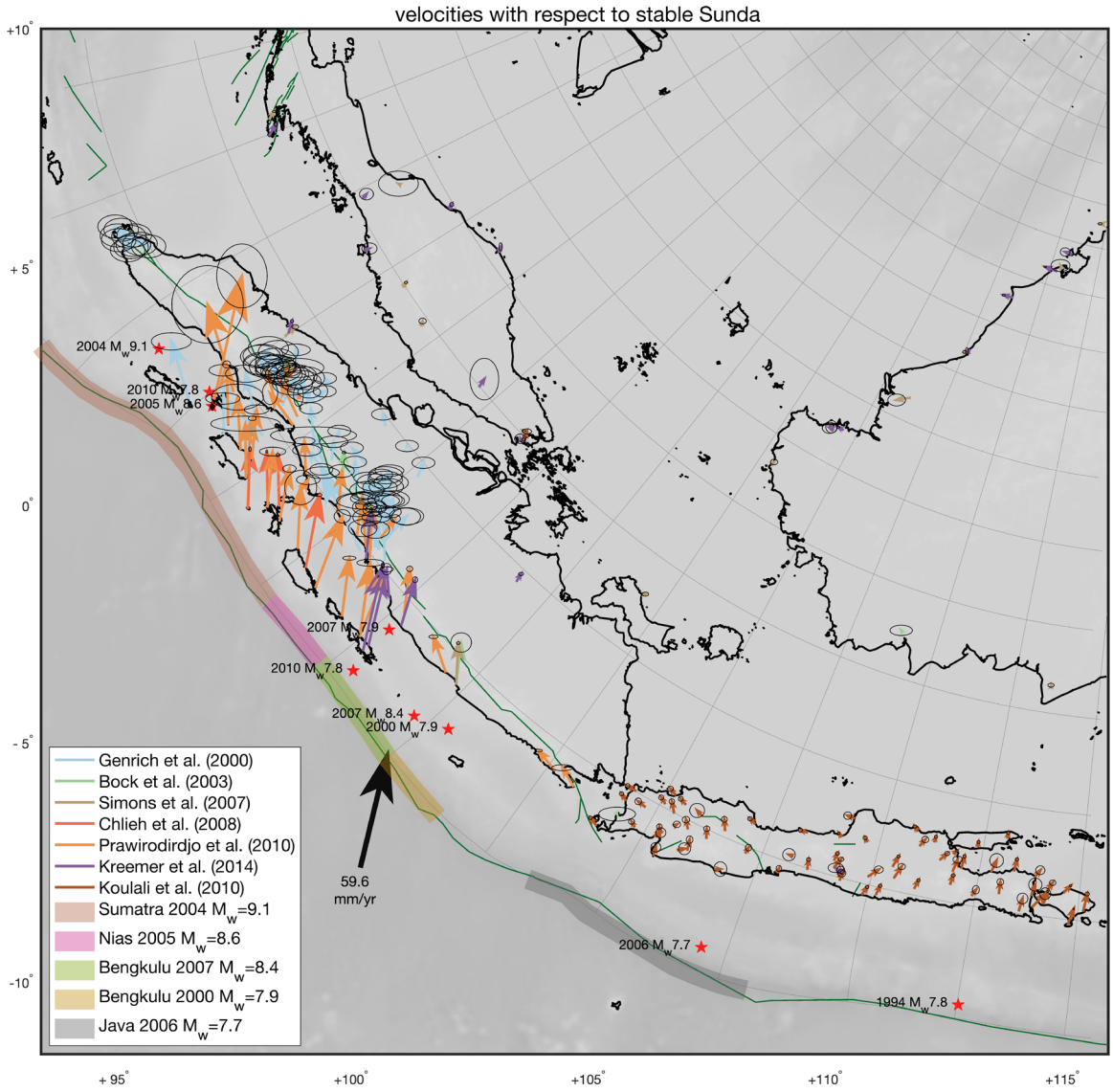
velocities with respect to stable Sunda
+10°
+ 5°
0°
- 5°
-10°
+ 95°
+100°
+105°
+110°
+115°
2004 Mw 9.1
2010 Mw 7.8
2005 Mw 8.6
2007 Mw 7.9
2010 Mw 7.8
2007 Mw 8.4
2000 Mw 7.9
59.6
mm/yr
2006 Mw 7.7
1994 Mw 7.8
Genrich et al. (2000)
Bock et al. (2003)
Simons et al. (2007)
Chlieh et al. (2008)
Prawirodirdjo et al. (2010)
Kreemer et al. (2014)
Koulali et al. (2010)
Sumatra 2004 Mw=9.1
Nias 2005 Mw=8.6
Bengkulu 2007 Mw=8.4
Bengkulu 2000 Mw=7.9
Java 2006 Mw=7.7

210

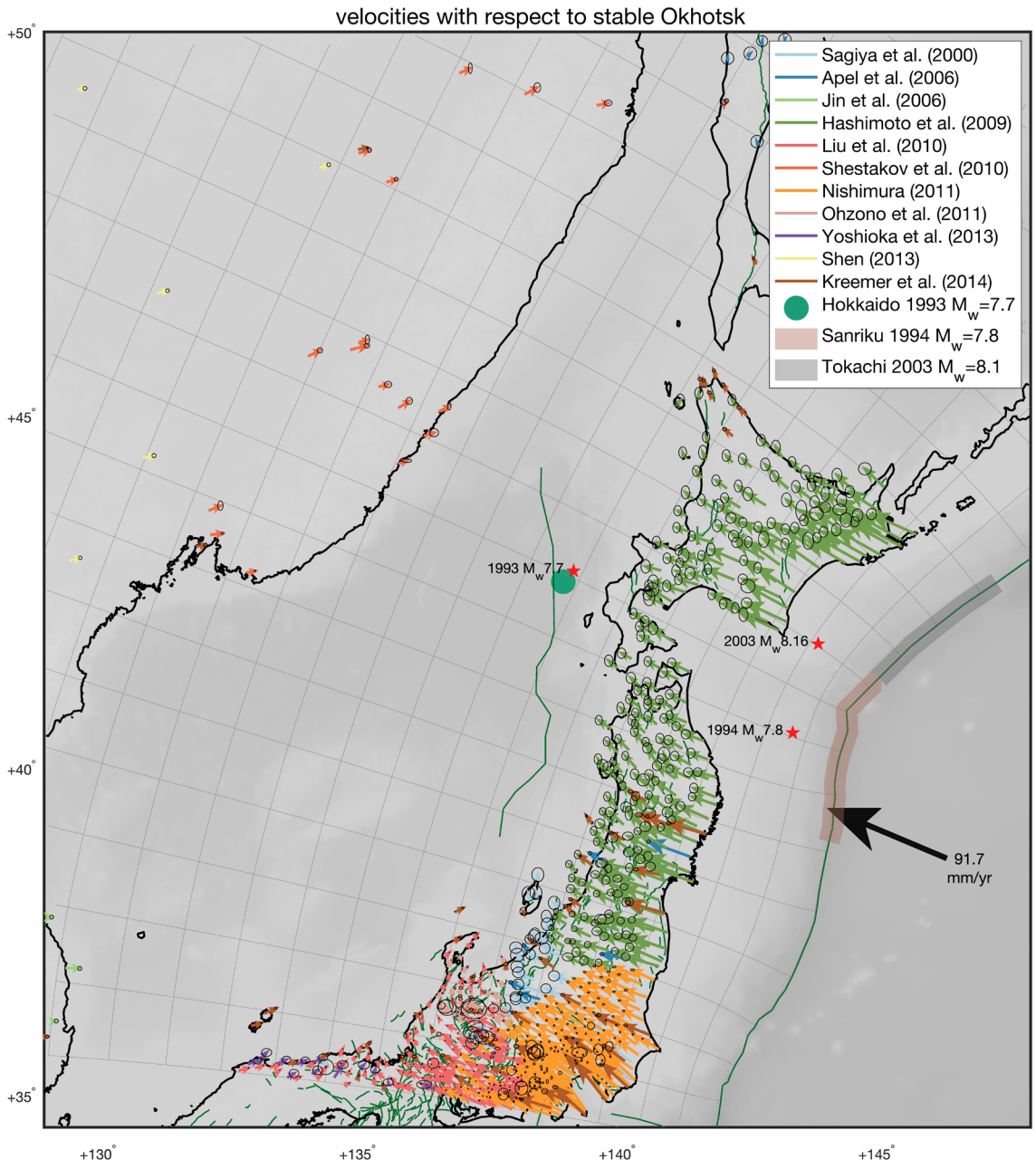

211

212 ***Figure 1.*** *Published observed velocities, topography, active faults (green), earthquakes with*
213 *M_w>7.5 during the time of observation (red stars), and trench-perpendicular/parallel orientations*
214 *(gray grid) in each of the three studied subduction zones. Interplate convergence velocities for the*
215 *Peru-Chile Trench, Sunda Trench and Japan Trench (pre-2011 Tohoku earthquake) are taken*
216 *from Kreemer et al. (2014), Simons et al. (2007), and Kreemer et al. (2014) (Okhotsk plate),*
217 *respectively. To exclude the effect of postseismic relaxation, in each segment of the subduction*
218 *zone that hosted a significant ($M_w \geq 7.5$) earthquake, we discard all velocities in the area that*

has been affected by coseismic displacements and postseismic transients (areas indicated by colored sections of the trench). For this reason we have a gap in the data distribution, as we exclude all data after the 1995 Antofagasta earthquake. Similarly, we exclude all data in southwest Hokkaido, where velocities increase towards the west, likely due to postseismic relaxation after the 1993 Hokkaido Nansei earthquake (Ueda et al., 2003). We set data exclusion zones stretching from the indicated parts of the trench to a distance from the trench (600 km and 1500 km for events larger than $M_w \geq 8.7$), which we apply to data collected after the events.

2.3 Interpolation of the decomposed velocity fields

Most geodetic studies of GNSS interseismic deformation have focused on deforming zones close to the margin for the purpose of estimating the megathrust locking pattern. In most regions, the geodetic benchmarks are unevenly distributed with much denser networks in near-trench areas than further away from the trench, and low density in the far-field plate interior that is used as the stable reference. For a continuous view on the velocity field and estimation of the location of velocity discontinuities, we separately interpolate the observed trench-perpendicular and -parallel velocity components. We account for the propagation of observational uncertainty, as well as for velocity variance in between observed sites, as follows. Under the assumption of local stationarity of the mean, variance and correlation of the velocity field, we use ordinary kriging (Wackernagel, 2003a), to interpolate and estimate uncertainties. We construct local correlograms that describe the local variability of the velocity field (Broerse et al., in prep.; Fouedjio and Séguret, 2016; Machuca-Mory and Deutsch, 2013). Further technical details are in Text S1 and Figures S1–S12.

2.4 Estimation of the hurdle location

The hurdle represents the main velocity discontinuity separating the interseismically deforming margin from the stable interior. The uncertainties of our interpolated velocity field represent both the data uncertainties, as well as the expected variance of the velocity field in between observation points. Supplementary figures S10–S12 show small velocity uncertainties in regions with little observed velocity variability, but a large increase of uncertainty with distance from observed points in regions where the data indicate a large gradient in velocities. Because of the adequate

uncertainty estimate, we can use the continuous interpolated velocity fields instead of the original observed point-wise velocities as basis for the spatially continuous estimate of the hurdle location.

First, we take equidistant trench-perpendicular profiles through the interpolated field. Trench-perpendicular and -parallel components along a profile, and their uncertainties, are estimated using bilinear interpolation. Subsequently, we fit a piece-wise continuous function consisting of two linear segments to the velocity as function of distance along the profile, using weighted non-linear least squares with a Trust Region algorithm and using inverse variances from the kriging as weights. The junction between the two segments represents the hurdle distance. We propagate the velocity uncertainties to the uncertainties of the hurdle location, approximated by linearization of the non-linear problem, for more details see the Supplement. Figures 2–4a,b show our estimated hurdle locations for each of the subduction zones. Figures 2–4c depict hurdle locations along selected trench-perpendicular profiles, next to interpolated velocities, their uncertainties, and GNSS observations.

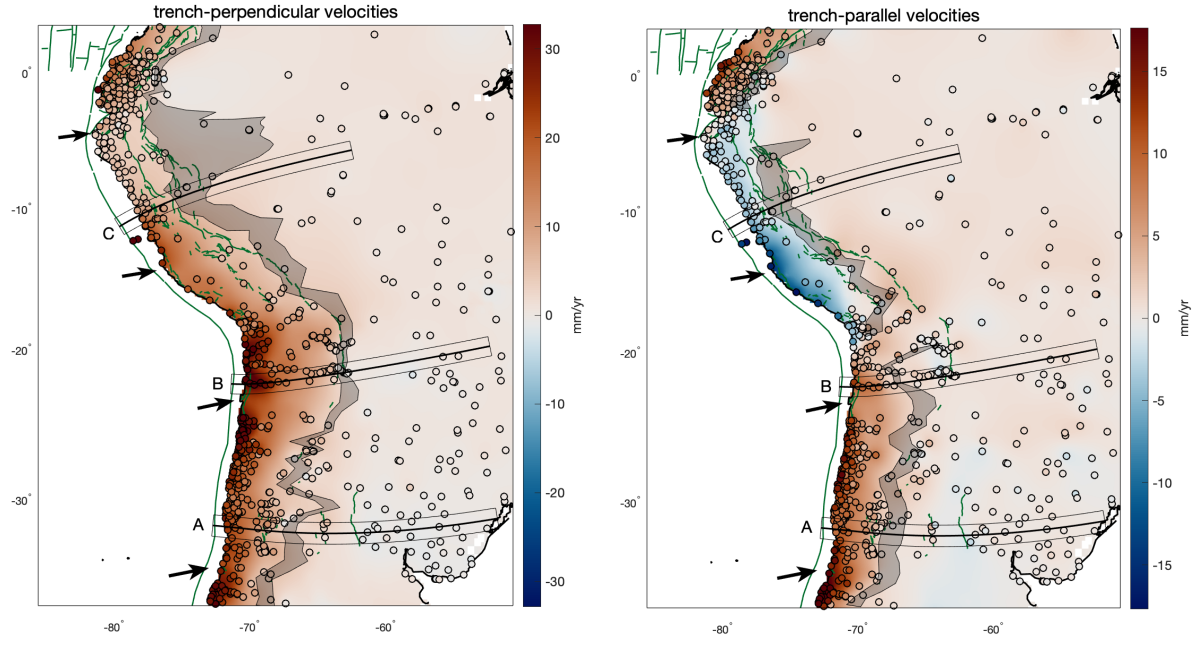

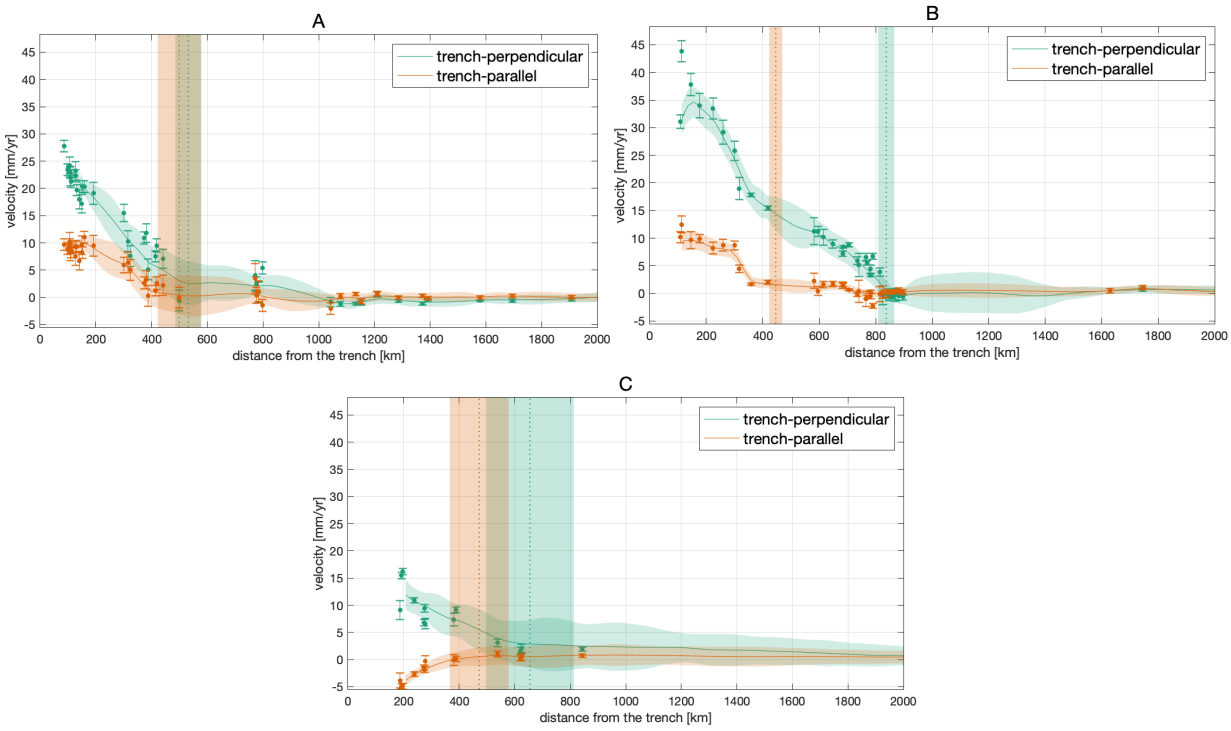

Figure 2. *The maps show interpolated interseismic velocity components (colors) for South America and the 95% confidence interval of the location of the hurdle in gray. Active faults from GEM (Styron & Pagani, 2020) are shown in green; on the left, we show trench-perpendicular velocities (positive landward), and on the right trench-parallel velocities (positive left-lateral). In both panels, circles represent benchmarks, and their fill color is the observed interseismic velocity. Arrows show the convergence direction along the Peru-Chile Trench* (Kreemer et al., 2014a). *Coastlines are drawn in black. Locations of trench-perpendicular swath profile lines A, B and C are shown on the maps by the thick line surrounded by the thinner lines showing the swath width. The panels below show the velocity profiles along A, B and C, including both interpolated velocity components with 1 standard deviation uncertainty (transparent bands), and the velocity components at GNSS stations within the swath with 1 standard deviation error bars. Note that the interpolated velocities are based on all GNSS velocity estimates, and not only those shown in the swath for reference. Vertical green and orange lines and bands outline estimated hurdle distances with 95% confidence intervals.*

279

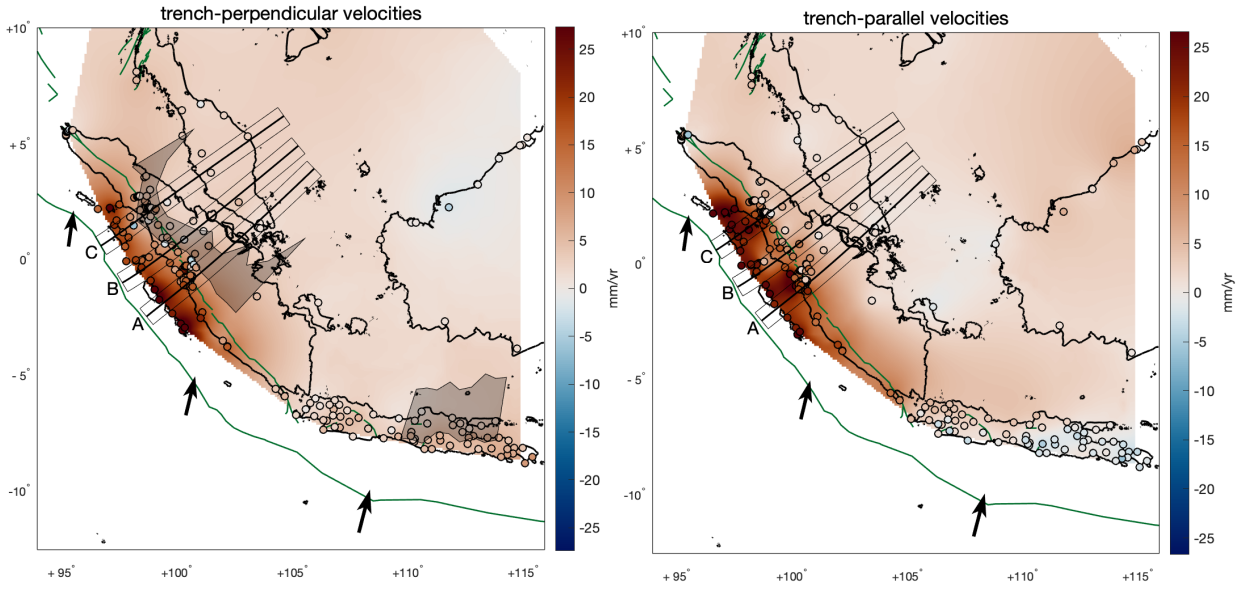

280

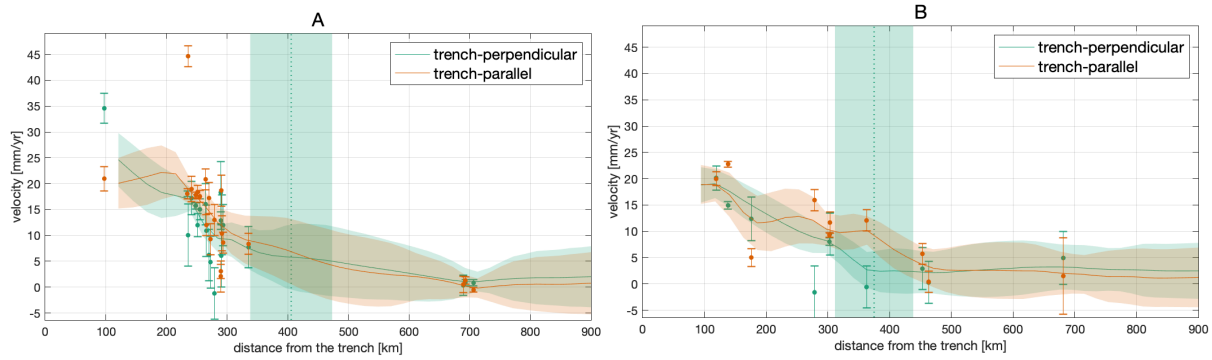

281

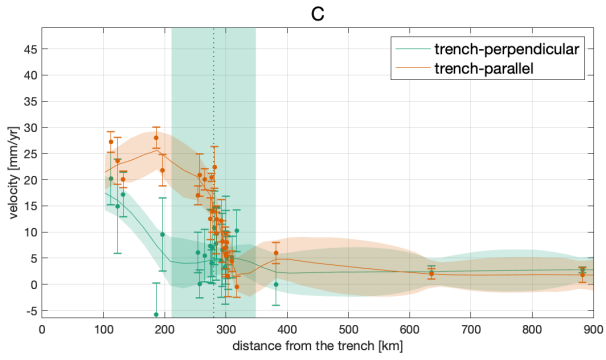

282 ***Figure 3.*** *The maps show interpolated trench-perpendicular (left panel, positive landward) and*
283 *trench-parallel velocity fields (right panel, positive left-lateral) and 95% confidence-interval*
284 *location of the hurdle (a,b), together with active faults in green from GEM (Styron & Pagani,*
285 *2020). Coastlines are in black and arrows show the interplate convergence direction between the*
286 *Sunda and Australian plates* (Simons et al., 2007a)*. Below, we show selected trench-perpendicular*
287 *velocity profiles (A–C) in Indonesia and Malaysia, on the landward side of the Sunda Trench,*

288 *along the profile lines shown and labeled in the maps. The velocity profiles show both interpolated*
289 *velocity components with 1 standard deviation uncertainty (transparent bands), and the velocity*
290 *components at GNSS stations within the swath with 1 standard deviation error bars. Note that the*
291 *interpolated velocities are based on all GNSS velocity estimates, and not only those shown in the*
292 *swath for reference. Vertical green and orange lines and bands outline estimated hurdle distances*
293 *with 95% confidence intervals.*

294

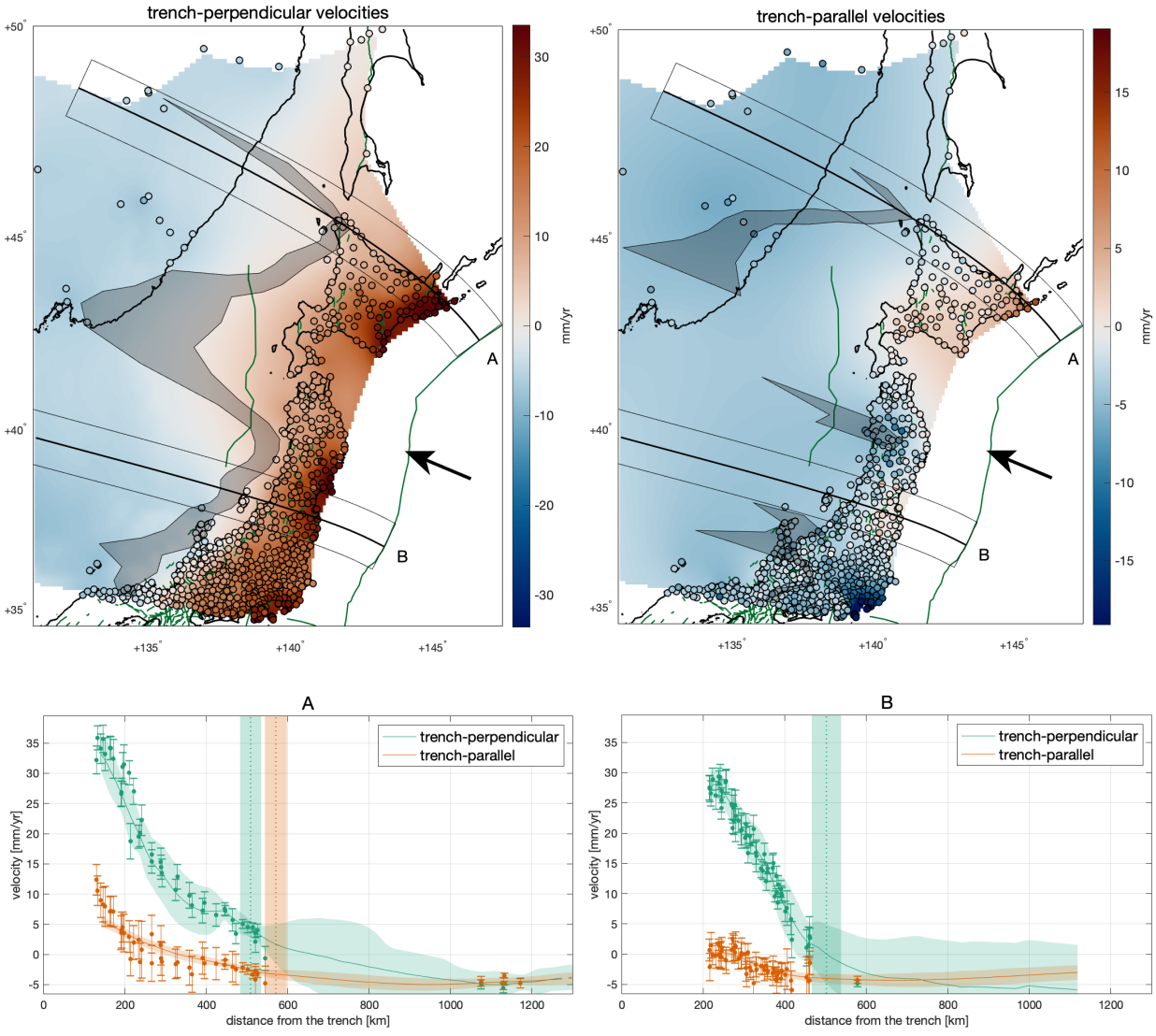

295

296

297 ***Figure 4.*** *The maps show interpolated trench-perpendicular (positive landward) and trench-*
298 *parallel (positive left-lateral) velocity fields with 95% confidence-interval location of the hurdle,*

together with active faults in green from GEM (Styron & Pagani, 2020). Coastlines are in black and arrows show the interplate convergence direction between the Pacific plate and Okhotsk (Kreemer et al., 2014a)*. Below, we show selected trench-perpendicular profiles, in Honshu and Hokkaido, on the landward side of the Japan Trench, along the profile lines traced in the maps. The velocity profiles show both interpolated velocity components with 1 standard deviation uncertainty (transparent bands), and the velocity components at GNSS stations within the swath with 1 standard deviation error bars. Note that the interpolated velocities are based on all GNSS velocity estimates, and not only those shown in the swath for reference. Vertical green and orange lines and bands outline estimated hurdle distances with 95% confidence intervals.*

2.5 Data analysis results

Both velocity components decrease approximately linearly with distance from the trench up to a hurdle, behind which a far-field region starts with low velocity amplitudes and gradients (see Figures 2–4). The hurdle location can be constrained best when both the velocity uncertainties are small, and there exists a strong discontinuity between the near-field and far-field velocity gradient. Trench-perpendicular velocities in particular show a steep near-trench decrease, except above sections of the megathrust that are not locked over an extensive trench-parallel distance. Such unlocked portions of the subduction interface are characterized by low interseismic velocity magnitudes (e.g., Matsu'ura & Sato, 1989), e.g., in northern Peru (4–9° S latitude) (Herman & Govers, 2020; Nocquet et al., 2014) and Java (Koulali et al., 2017a). Trench-parallel velocities show a more complex behavior, particularly where the convergence obliquity changes direction (inverting the sign of near-trench trench-parallel velocities) and forearc slivers have been suggested to exist (Herman and Govers, 2020; Métois et al., 2016; Nocquet et al., 2014a). Nevertheless, trench-parallel velocities also indicate a hurdle, beyond which amplitudes are near-zero and the slope is very shallow.

In South America, we can identify the trench-perpendicular hurdle as the location of the transition between rapid near-trench decay and the other, shallower slope in the far-field. The hurdle is located at distances from the trench varying between 400 and 1000 km approximately, including the lower and upper bounds of the confidence interval, except for the section of subduction zone with poorly coupled megathrust in Northern Peru (4–9° S) (Figure 2). The hurdle location generally largely tracks the eastern margin of the Andean orogen (Figure 5a). Only landward of

the poorly locked megathrust of Norther Peru, the trench-perpendicular gradient in the velocity component is low and the hurdle location is identified at distances beyond 1000 km from the trench, although the uncertainty on the location is very large and the nearest location within the confidence interval still tracks the eastern boundary of the orogen. The hurdle lies a few tens of km landward of the backthrust in south-central Peru (10–13° S). Further to the south, in Bolivia (14–21°), it precisely follows the backthrust at the base of the mountain range. In northernmost Argentina there is no clear, active backthrust, but the hurdle traces the border of the Puna plateau. Immediately to the south, around 30° S, the hurdle is located in the middle of the Sierras Pampeanas.

For South America, the hurdle for trench-parallel velocities is located between 220 and 800 km from the trench, excluding the poorly coupled megathrust section. It is always closer to the trench or coincident with the trench-perpendicular hurdle. Velocities beyond the hurdle are near, but not always exactly, zero: the trench-perpendicular component is between -1 and 4 mm/yr in amplitude, while the trench-parallel component is between -1 and 2 mm/yr.

Observations of interseismic velocities in Sumatra are sparser than in South America. In the southeast of the island, observations are far apart. Both velocity components are small and have low gradients, including the near-trench region (Figure 3). This reflects the low coupling in that region (Chlieh et al., 2008a) and does not allow us to locate any hurdle. In central Sumatra, where near-trench velocities indicate strong interplate coupling and data coverage is much denser, we observe a hurdle in the trench-perpendicular component, bounding the zone of near-uniform low velocities in the interior of Sunda (Simons et al., 2007a). The hurdle runs through the middle of the island, roughly coinciding with the southwestern edge of the Sibumasu terrane reported by Hutchison (2014) and Metcalfe (2011) (Figure 5b), as well as with the northeastern boundary of the zone of active orogenic deformation as indicated by Hall and Sevastjanova (2012). Trench-parallel velocities do not show a uniform decrease with distance from the trench, but rather are near-uniform on the Indian Ocean coast of central Sumatra and in the smaller offshore islands, and have a strong gradient over the Sumatran Fault (Genrich et al., 2000a; Prawirodirdjo et al., 1997), behind which the parallel velocities quickly converge to zero. We thus do not perform our parallel hurdle location estimation in Sumatra. In Java, both velocity components are low throughout, indicating low megathrust coupling (Koulali et al., 2017a), and the lack of observations to the northeast of the island, in the Java Sea, prevents us from confidently identifying a hurdle.

Along the Japan trench, trench-perpendicular velocities decrease with distance from the trench following a steep trend with constant or gently decreasing slope in the vast majority of Hokkaido (trench locations north of 42° N) and most of central-northern Honshu (south of 40° N). The resulting hurdle location measures ~450–600 km from the trench (Figure 4). It broadly follows the eastern margin of the floor of the Sea of Japan, a few tens of km offshore except for where it touches the northernmost tip of Hokkaido (Figure 5c). On the other side of the Sea of Japan, observations in Manchuria and South Korea constrain the velocity field at intermediate to far distances, helping locate the hurdle. The trench-perpendicular and trench-parallel velocities in those sites are uniformly negative (around 5 mm/yr, both trenchward and right-lateral, respectively), indicating limited transpressional motion between Manchuria, inferred to be part of the Amurian plate, and Hokkaido, generally considered part of the Okhotsk plate (Petit and Fournier, 2005; Weaver et al., 2003). Off the shore of south-central Honshu (south of 40° latitude), observations in the intermediate- and far-field are not available and the velocity filed in the Sea of Japan is interpolated relying on observations far to the northwest. Nevertheless, the steep, near-linear decrease of trench-perpendicular velocities in the densely instrumented island convincingly supports the existence of a hurdle. The Okhotsk-Amurian plate boundary, inferred here to cross Honshu by Bird (2003), does not affect the slope of trench-perpendicular velocities with distance from the trench. In northernmost Honshu and the southwestern most tip of Hokkaido (for trench locations between 40° and 42° N), both the trench-perpendicular velocities and their trench-perpendicular gradients are lower, possibly reflecting lower interplate coupling than in laterally adjacent portions of the megathrust (Hashimoto et al., 2009a; Suwa et al., 2006) or incomplete postseismic transient corrections for the 1994 Sanriku earthquake (Loveless and Meade, 2010).

Trench-parallel velocities in northern Honshu are low, while the uncertainties of available interseismic velocities are relatively high. This, combined with the narrow width where observations are possible, makes it difficult to identify a hurdle in the trench-parallel component. Additionally, trench-parallel velocities vary in sign across the study area. This clearly reflects in part small changes in the strike of the trench which, combined with the overall head-on character of the convergence, changes the sign of the trench-parallel component of the velocity of the downgoing (Pacific) plate with respect to the overriding (Okhotsk) one. Nevertheless, trench-parallel velocities seem to decrease to uniform values (-5–-6 mm/yr, reflecting the northwards

motion of the Amurian plate with respect to the Okhotsk) within ~600 km of the trench in northern Hokkaido and within ~300–400 km in northern Honshu.

We also performed the data analysis for Japan expressing all velocities with respect to the Amurian plate, rather than the Okhotsk plate, see supplemental figure S13. This uniformly increases trench-perpendicular velocities by ~6 mm/yr and the trench-parallel by ~5 mm/yr. Trench-perpendicular velocities are thus entirely positive (landward), while trench-parallel velocities are largely positive (dextral). Only a few areas with negative trench-parallel velocities remain: some isolated near-zero negative patches and the southeastern corner of Honshu, next to the Sagami Trough and the assumed southern boundary of the Okhotsk plate. The estimated trench-perpendicular hurdle location is completely unaffected by shifting the reference frame from the Okhotsk- to the Amurian plate. Conversely, the change in reference frame allows for determination of the hurdle in the trench-parallel component within our uncertainty threshold, by reducing the far-field variability in amplitudes and thus the interpolation uncertainty. The resulting hurdle is located ~260–450 km from the trench off the coast of Honshu and 560–870 km from the trench off Hokkaido, with the largest values for profiles in southern Hokkaido, where the velocities are uniformly higher on the island than in the mainland.

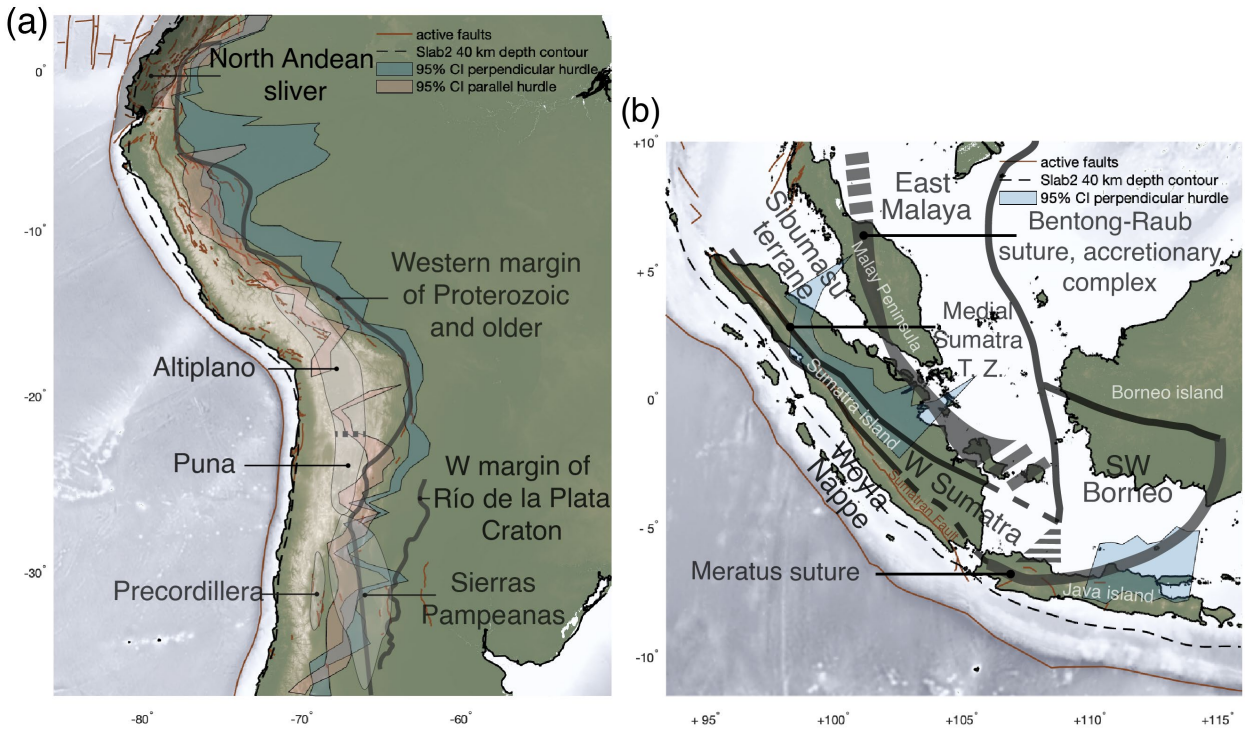

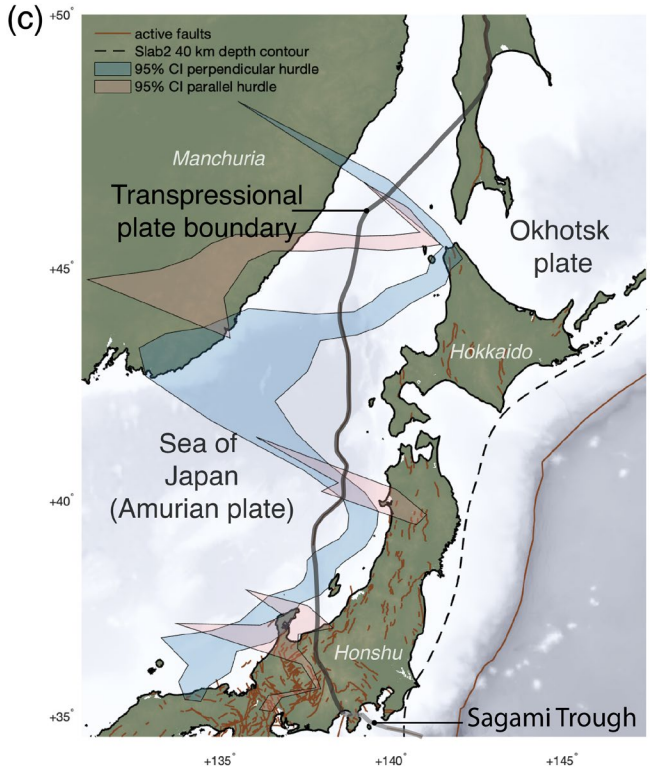

408

409 ***Figure 5.*** *Location of both hurdles against topography, active faults (green), 40 km depth contour*
410 *of the top of the slabs (megathrust) (Hayes et al., 2018), and major tectonic and geological features*
411 *discussed in the main body, for each of the three study areas. Dashed lines indicate inferred or*
412 *disputed locations. (a) For South America, the eastern front of the Precordillera, the broad*
413 *location of the Sierras Pampeanas, and the western edge of the Río de la Plata Craton are taken*
414 *from Álvarez et al. (2012), while the orange line marks the approximate extent of the Proterozoic*
415 *and older crustal domains (Chulick et al., 2013). (b) For Sunda, the location of the Meratus suture*
416 *and Southwest Borneo crustal block is taken from Haberland et al. (2014) and Metcalfe (2011),*
417 *while the Medial Sumatra Tectonic Zone and the crustal domains in Sumatra and the Malay*
418 *peninsula are taken from Hutchison (2014) and Metcalfe (2011). (c) For Japan, plate boundaries*
419 *are from Bird (2003).*

420

421 *2.6 Discussion and conclusions of the data analysis*

422 Trench-perpendicular velocities decrease with distance from the trench in a broadly linear fashion
423 up to the hurdle. Beyond the hurdle, perpendicular velocities and gradients are distinctly lower.
424 The hurdle in trench-perpendicular velocities is located within 1000 km or less of the trench along

the three studied subduction zones. Trench-parallel velocities sometimes have complex patterns, partly due to curvature of the margin. In South America, parallel velocities generally also decay steeply with distance, up to a hurdle that roughly coincides with the trench-perpendicular hurdle or that is located up to several tens of km closer to the trench. Hurdle locations broadly, but not precisely, follow the inland boundary of the orogen located along the margin, where a clear boundary exists.

The sharp decrease to (near-)zero of trench-perpendicular interseismic velocities was first noted by Norabuena (1998) for the northern portion of the Central Andes (the Altiplano of Peru and Bolivia) and Brooks et al. (2003) for the Southern Andes. The authors explain the observations by active back-arc convergence or sliver motion, which has remained a popular explanation (Bevis et al., 2001; Brooks et al., 2011a, 2003a; Herman and Govers, 2020; Kendrick et al., 2006; McFarland et al., 2017a; Métois et al., 2013a; Shi et al., 2020; Weiss et al., 2016a). The interpretation involving active backthrusts implies that interseismic strain accumulation by slip on a backthrust system involves non-recoverable strain by fault slip or deep shear zones. The fold-and-thrust belt at the eastern margin of the Altiplano-Puna plateau, at roughly 11–22° S latitude, is bounded by a well-defined thrust front and is indeed considered to be actively deforming, despite little recent seismic activity (Brooks et al., 2011a; Wimpenny et al., 2018). Farther north in Peru (4–11° S) and farther south in Argentina (around 31° S), moderate instrumentally-observed earthquakes and strong historical earthquakes indicate that some fraction of permanent strain occurs by thrust and reverse faulting in the eastern foreland of the Andes (Alvarado and Ramos, 2011; Jordan et al., 1983; Rivas et al., 2019; Sébrier et al., 1988). However, active and continuous backthrusts faults appear to be absent in some locations along the Andean orogen and the other two subduction zones we study, specifically at 22–29° S and south of 32° S latitude in South America, throughout Sumatra and Java, and south of 39° N and north of 45° N off the west coast of Japan. Elsewhere, in the Sea of Japan, the inferred active faults accommodating convergence between the Okhotsk and Amur plates do not coincide with the location of the hurdle (Figures 1–4).

Even where active backthrusts are observed, their role in explaining the spatial distribution of surface velocities may have been misinterpreted because of unrealistic model assumptions. Most studies that numerically model the effect of back-arc convergence on interseismic velocities assume a fully elastic Earth during the entire earthquake cycle, which strongly underestimates far-field horizontal velocities and can lead to mistaken interpretations of observations (Li et al., 2015;

Trubienko et al., 2013). Shi et al. (2020) do use a visco-elastic rheology, but their model artificially imposes zero horizontal motion at a horizontal distance of ~950 km from the trench, i.e. only ~150 km farther than the back-arc thrust front. Additionally, their decrease in modeled trench-perpendicular velocities with distance from the trench is less linear than observed, while their backthrust produces only local offsets in velocities, above the backthrust. Furthermore, most of the modeling studies invoking back-arc convergence require basal detachment faults extending in the trench-normal direction for ~200 km or more (Brooks et al., 2011a; McFarland et al., 2017a; Shi et al., 2020; Weiss et al., 2016a). This may be unrealistic, considering that the E-W extent of the central Andean back-arc fold-and-thrust belt that is currently geologically active is only ~70 km wide (Pearson et al., 2013). Other authors treat the contact between the Andean orogen and the interior of South America as a plate boundary, implying that this boundary cuts through the entire lithosphere, slipping freely at depth, and is laterally continuous all along the orogen. Because of the extreme spatial extent and continuity of the modeled thrusts or plate boundaries, these studies probably overestimate the geodetic imprint of the localized shortening at the eastern edge of the Andes. Additionally, none of the aforementioned studies investigating the spatial distribution of interseismic velocities consider whether significant far-field coseismic displacements can be explained by their models. Within the framework of the earthquake cycle, we think there should be consistency in terms of coseismic slip and slip deficit accumulation, response of backthrust slip and creep to the stress evolution during the cycle, and boundary conditions.

Active faults are the possible cause of hurdle behavior in some regions. North of ~2° S in South America, in southern Ecuador and Colombia, convergence is highly oblique and subparallel to a system of strike-slip and thrust faults (Veloza et al., 2012) that roughly coincides with the location of the hurdle in both velocity components. Localization of interseismic velocities might be chiefly caused by the fault system, consistently with the interpretation of this fault system as bounding a distinct, internally deforming North Andean sliver (e.g., Alvarado et al., 2016; Kellogg et al., 1995; Nocquet et al., 2014; White et al., 2003). In Sumatra, trench-parallel velocities seem to be governed by the active strike-slip Sumatran Fault (Genrich et al., 2000a; Prawirodirdjo et al., 1997). Trench-parallel velocities also suggest localized strike-slip motion between southern Hokkaido (on the Okhotsk plate per Bird, 2003) and northern Manchuria (on the Amurian plate), but the lack of GNSS observations in the Sea of Japan precludes a specific localization of the boundary from a

purely geodetic perspective. The complex pattern of trench-parallel velocities in Japan, with changes in sign along the trench, might indicate internal tectonic deformation within the islands.

Trench-perpendicular velocities in all three study areas show a consistent steep decrease with distance from the trench. Trench-parallel velocities in South America, away from the North Andean sliver, show a similar trend. This suggests a more universal cause of the observed hurdles than fault zones. We find no correlation between shallow megathrust dip and hurdle location, since the dip changes very little along the studied trenches (Figure 5). We therefore focus on a possible explanation involving the overriding plate. Although the thrust faults in the Andean back-arc are unlikely to directly account for the decrease in observed velocities as we move away from the trench, they are likely associated with a mechanical contrast between the deformed and partly accreted Andean region and the interior of the South America plate. We thus hypothesize that such a contrast exists in this and other subduction zones, that it is responsible for the behavior of interseismic velocities, and that a uniform overriding plate cannot account for observations.

The effective elastic thickness T_e derived from flexure observations is much lower at the margin than in the interior of South America (Pérez-Gussinyé et al., 2008, 2007; Stewart & Watts, 1997). Variations in effective elastic thickness may derive from variations in thickness, composition, temperature, rheology, and on the age of the load (Burov & Diament, 1995; Watts, 1981). The effective elastic thickness is derived from lithospheric flexure on geological time scales and is not directly applicable to the predominantly horizontal plate loading over interseismic timescales. It is very likely however that a relevant mechanical contrast exists. The load-bearing capacity of the low-viscosity mantle wedge is negligible on (interseismic) time scales, meaning that the contrast must be related to properties of the overriding plate. The bulk of the interseismic shortening of the overriding plate is recovered during megathrust earthquakes, so it can be considered largely elastic. A mechanical contrast that is relevant in the context of earthquake cycles is thus a compliance contrast or thickness contrast. Below we present mechanical models aimed at exploring our hypothesis that (interseismic) hurdles are a consequence of such contrast, whilst also showing significant coseismic displacements beyond the hurdle.

The presence of stiff cratonic lithosphere in the interior of the South American plate in central Argentina was proposed as the explanation for the relatively low horizontal postseismic velocities in the region (compared to model results without such a craton) by Klein et al. (2016). Itoh et al.

(2019) instead showed that a compliant arc and back-arc region can explain the high gradient of onshore horizontal interseismic velocities with distance from the trench in Hokkaido. We hypothesize that a mechanical contrast between more compliant lithosphere at the convergent margin of the overriding plate (in the arc and back-arc region) and less compliant, more rigid lithosphere of the interior of the plate can explain the observed near-trench localization of high spatial gradients of horizontal surface velocities. We thus propose that such a contrast, avoiding artificially fixed model edges in the vicinity of the trench, can produce a hurdle in interseismic velocities and surface motion generally consistent with observations throughout the seismic cycle, even though we specifically focus here on interseismic observations.

3 Numerical model

3.1 General concept

To study the interseismic and coseismic surface deformation field we develop a three-dimensional (3D) mechanical model. We seek to explain observation trends at different margins, i.e., the semi-linear decrease of interseismic velocities from the trench to the hurdle, the low interseismic strain accumulation beyond it, but significant far-field coseismic displacements due to a megathrust earthquake. We test whether these trends may be a consequence of a compliancy contrast in the overriding plate. In the context of our model, we use a contrast in Young's modulus E and shear modulus G, with the same ratio between the two moduli, in an overriding plate with a uniform thickness and poisson's ratio ν. Rather than representing realistic averages of the elastic properties of the lithosphere, the model Young's modulus values proxy for a more general ability of the plate to resist intraplate stresses resulting from the total thickness, composition, and thermal state of the real lithosphere. The modeled contrast in the elastic properties of the overriding plate consists of a relatively low Young's modulus in the "near-trench" region and a higher modulus in the far-field. The assumed geometry of the slab and overriding plate in the model is not specific for any margin and instead follows a realistic trench-perpendicular slab profile (Figure 6). We consequently do not expect to reproduce specific regional observations with the model.

Model deformation is driven by slab motion and sporadic unlocking of asperities. Govers et al. (2018) show that coseismic slip increases per earthquake cycle until a dynamic steady state is reached with physically consistent prestresses.

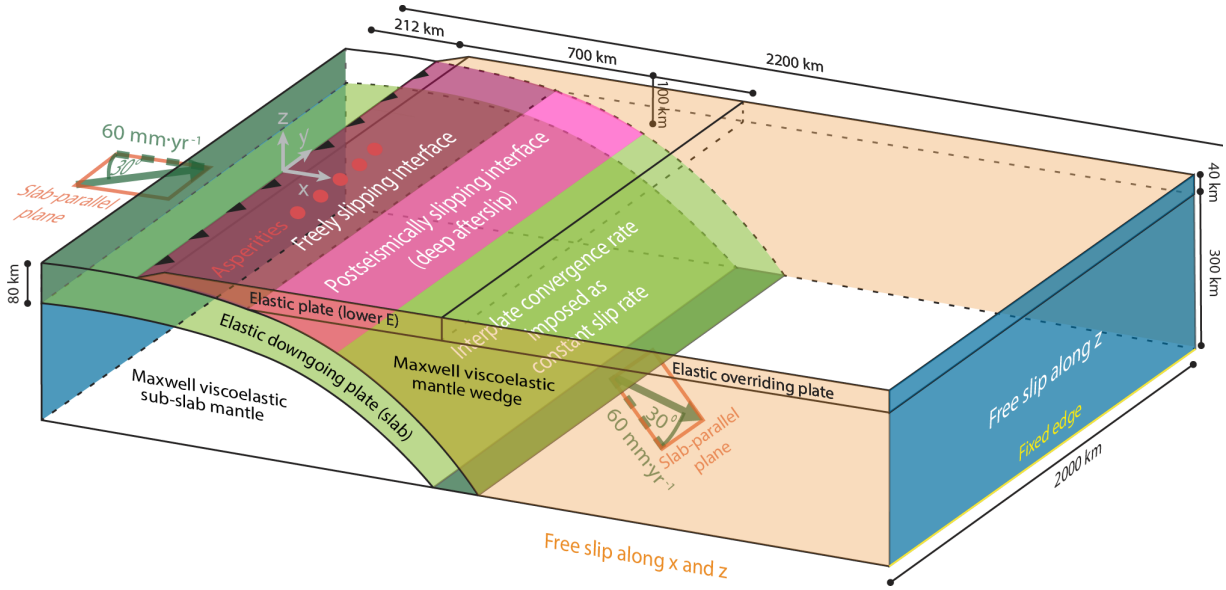

Figure 6. *Schematic representation of the model domain with its geometry, spatial extent, coordinate system, main mechanical properties, and the applied boundary conditions.*

3.2 Model domain and rheology

We have chosen the model domain size so that boundaries and boundary conditions do not affect the results in our region of interest; the trench-perpendicular (x) model extent is 2200 km, 2000 km in the trench-parallel direction (y) direction, and 388 km in the depth (z) direction. The trench is located at $x = 0$, while the oceanward model boundary is located at x=-212 km. The surface downgoing plate has its upper surface at a depth of 8 km, and the overriding plate at z=0. The subducting plate has a thickness of 80 km, consistent with the seismologically detected depth of the lithosphere-asthenosphere boundary of various oceanic plates (Kawakatsu et al., 2009; Kumar & Kawakatsu, 2011). The overriding plate has a uniform 40 km thickness, except at the taper due to the megathrust geometry at the bottom and at the slope down to the trench over 18 km horizontal distance.

The model slab and the overriding plate are elastic, and the mantle wedge and sub-slab asthenosphere are viscoelastic with a Maxwell rheology. We model seismic cycles with quasi-dynamic slip on discrete faults and shear zones (see Section 3.4, as well as Section 2 of Govers et al., 2018). After model spin-up, the model has identical megathrust earthquake cycles with a return period of 300 years. Postseismic relaxation in the model involves the two most relevant large-scale

processes, afterslip and viscous relaxation (Broerse et al., 2015; Bürgmann and Dresen, 2008; Diao et al., 2014; Klein et al., 2016). Our reference model has a mantle viscosity of 10^{19} Pa·s. Throughout the model domain, outside of the overriding plate, the elastic moduli are uniform: Poisson's ratio ν is 0.25 and Young's modulus E is 100 GPa, consistently with values from PREM (Dziewonski and Anderson, 1981a) in the 0–40 km depth range. In particular, the ν value of 0.25 consists of the common Poisson solid assumption (e.g., Melosh and Raefsky, 1983) and is very consistent with the values determined for lower crustal and mantle lithologies, while being at the lower end of the realistic range for the upper crust . The return period thus is ~37.9 characteristic relaxation (Maxwell) times long, so that about 55% of the model cycle period is interseismic, given that the earthquakes on the different asperities within one cycle occur within 40 years of each other (Govers et al., 2018).

3.3 Numerical method

We use a finite element method to solve the 3D mechanical equilibrium equations for given material properties and boundary conditions including a free surface, as detailed below. Finite element platform *GTECTON* version 2021.0 uses the Portable, Extensible, Toolkit for Scientific Computation (*PETSc* version 3.10.4; Balay et al., 2021a, 2021b, 1997) and *OpenMPI* (version 3.0.0; Gabriel et al., 2004) to solve the time-dependent mechanical problem in parallel (e.g., Govers et al., 2018; Govers and Wortel, 2005).

Each model includes 384,566 nodes, 2,238,109 elements and 1,284,193 total degrees of freedom. These choices are based on pilot models to find a mesh where surface deformation is insensitive to further grid refinement. A posteriori estimates of the model error (Verfürth, 1994) for the selected mesh are small enough to support our conclusion that our results are accurate within a few %.

3.4 Modeling the megathrust

Dynamic differential slip on the megathrust is modeled using the slippery nodes technique (Melosh & Williams, 1989). Five asperities on the otherwise freely-slipping megathrust are fully coupled/locked during all stages of the earthquake cycle except during the coseismic stage when

596 unlocked asperities can slip freely. Treating the megathrust away from the asperities as freely
597 sliding is consistent with observations of megathrust regions immediately up- and downdip of the
598 asperities sliding stably and with low friction (Hardebeck, 2015; Ikari et al., 2011; Scholz, 1998).
599 The asperities are circular in map view and have a diameter of 50 km, which is consistent with
600 inversion results of (Herman and Govers, 2020). They are centered at a horizontal distance of 120
601 km from the trench and 100 km from each other, resulting in pseudo-locking and accumulation of
602 slip deficit over an along-trench distance of ~500 km (Herman et al., 2018). The middle asperity
603 is first unlocked to allow (coseismic) slip in each new cycle. After a delay of 20 years, the
604 intermediate asperities are unlocked. After 20 more years, the outer asperities are unlocked.

605 Coseismic slip, although traditionally thought to not extend to very shallow depth as a result of the
606 unconsolidated material in the hanging-wall (Kanamori, 1972; Moore & Saffer, 2001), can indeed
607 propagate up to the trench (Fujiwara et al., 2011; Sladen & Trevisan, 2018). We apply velocity
608 strengthening in the form of (small) shear tractions that are proportional to the amount of coseismic
609 fault slip, with a spring constant of 200 Pa/m. This way, we allow (while minorly restricting)
610 coseismic slip on the updip portion of the megathrust, above 15 km depth. Downdip of the
611 megathrust, the contact between the subducting plate and the mantle wedge (depths >40 km in our
612 models) is commonly thought to be a viscoelastic shear zone (van Keken et al., 2002; Tichelaar &
613 Ruff, 1993). In our model, we represent it as an infinitely thin shear zone that is elastic
614 coseismically and resembles low-viscosity behavior during other periods of the earthquake cycle
615 by slipping freely via slippery nodes. The shear zone thus fully resolves coseismic stress changes
616 during an instantaneous primary afterslip phase and creeps with no resistance interseismically.
617 This implementation has the significant benefit of avoiding the computationally demanding
618 simulation of viscous flow in a narrow channel, while capturing the main features of interseismic
619 and coseismic behavior and producing afterslip. Govers et al. (2018) used a similar approach, and
620 they defined “primary afterslip” as immediate viscous slip on the shear zone in response to
621 coseismic stress changes that is generally thought to occur much more quickly than bulk viscous
622 relaxation in the mantle wedge (Govers et al., 2018a; Muto et al., 2019). “Secondary” afterslip
623 refers to slip on the deep shear zone in response to stress redistribution during the postseismic
624 phase.

625 Afterslip on the deep shear zone is commonly assumed to occur at depths shallower than about
626 80–100 km (Diao et al., 2014; Freed et al., 2017; Hu et al., 2016; Sun et al., 2014; Yamagiwa et

627 al., 2015). Klein et al. (2016) showed that allowing relative motion between the mantle wedge and
628 the slab, by introducing a narrow low-viscosity zone between 70 and 135 km depth along the top
629 of the slab, produces little change in postseismic horizontal surface motion. In our model, we
630 therefore allow afterslip, and interseismic slip deficit accumulation, on the shear zone downdip of
631 the megathrust only at depths smaller than 100 km.

632 We aim to capture deformation and flow of the mantle wedge and asthenosphere in response to
633 stress changes during the earthquake cycle. To exclude modeling steady-state mantle flow on
634 geological time scales that is irrelevant for the seismic cycle, we use the finite element split node
635 technique (Melosh & Raefsky, 1981) to impose the slab velocity beyond a depth of 100 km.
636 Similarly, we avoid driving long term sub-slab asthenosphere by applying the slab velocity along
637 the base of the slab. We remove a small residue of long-term deformation of the model related to
638 stretching and unbending of the slab that we identify from an identical model without asperities or
639 earthquakes. This approach facilitates loading of the mantle wedge and sub-slab asthenosphere by
640 non-steady velocity/stress perturbations during all stages of the earthquake cycle.

641

642 *3.5 Boundary conditions*

643 We impose the updip and downdip ends of the downgoing plate to move obliquely at the interplate
644 velocity in the direction parallel to the slab surface. The trench-perpendicular component of the
645 velocity is 60 mm/yr, while the trench-parallel component (34.64 mm/yr) is such that the total
646 velocity is at a 30° angle (counter-clockwise), in a slab-parallel plane, to the trench-perpendicular
647 direction (Figure 6). We have verified that the presence and magnitude of the trench-parallel
648 velocity does not affect trench-perpendicular late interseismic surface velocities or coseismic
649 surface displacement. We apply a free-slip boundary to the remaining lateral, vertical sides of the
650 model, while we allow only vertical motion at the landward end and fix the bottom landward and
651 oceanward edges of the vertical sides.

652 Restoring pressures impose isostasy along the free surface of both plates (Govers and Wortel,
653 1993a). These pressures act perpendicularly to the surface and have a magnitude directly
654 proportional to displacement in that direction. The constant of proportionality is the gravitational
655 acceleration (9.8 m/s^2) times the density contrast—3250 kg/m^3 at the top of the overriding plate,
656 2200 $kg \cdot m^{-3}$ at the top of the oceanic plate.

657 **4 Modeling results and analysis**

658 *4.1 Reference model*

659 In our reference model, the overriding plate has a Young's modulus of 50 GPa within 700 km
660 horizontal distance from the trench, while the remainder of the overriding plate has a Young's
661 modulus of 250 GPa. Figure 7 shows the resulting surface deformation. Figure 7a and 7c show
662 interseismic velocities for 260 years after the last earthquake on any asperity, i.e., after ~33
663 Maxwell times. Both the trench-perpendicular and trench-parallel velocity components decrease
664 with distance from the locked asperities. The transect through the central asperity in Figure 7c
665 (solid line) shows a roughly linear decrease in the trench-perpendicular velocity with distance from
666 the trench, from the peak value (above the asperity) to the location of the contrast, where the
667 gradient decreases sharply. Here, the trench-perpendicular velocity is ~10% of the interplate
668 convergence rate and ~8% of the peak value. Beyond the contrast, the trench-perpendicular
669 velocity in the far-field decreases gradually to zero at the far end of the model, which is a
670 consequence of the model boundary condition there. Trench-parallel velocities along this transect
671 instead decay with a progressively shallower slope away from the peak (Fig. 7c). They reach a
672 near-zero value at the compliance contrast and reach ~10% of the peak value ~200 km closer to
673 the trench. The steeper decrease in the trench-parallel component causes velocity directions in the
674 locked portion of the subduction zone to rotate from convergence-parallel to trench-perpendicular
675 with distance from the trench (Figure 6a). The results thus show slow and mostly trench-
676 perpendicular interseismic strain accumulation beyond the contrast. The mechanical contrast thus
677 results in hurdle-type behavior comparable to what we infer from the GNSS data. The hurdle is
678 expressed in both horizontal velocity components, albeit more clearly in the trench-perpendicular
679 velocities.

680 Interseismic velocities 500 km to the north of the middle of the model (Fig.7a and 7c) are
681 substantially slower than above the central asperity. They are higher than velocities 500 km to the
682 south of the central asperity, showing that oblique convergence results in a distinctly asymmetric
683 pattern of interseismic strain accumulation. Particularly the trench-parallel velocity differs.
684 Trench-parallel velocities along the northern transect in Figure 7a and 7c increase with distance
685 from the trench before decreasing again. Figure 7a shows that, in a trench-perpendicular profile
686 500 km the south of the middle of the model, trench-parallel velocities decrease with distance from

the trench. Trench-perpendicular velocities on both lateral sides decrease with distance from the trench. The imprint of the contrast on the (gradient of the) velocities is less pronounced away from locked asperities than in the central region.

Unlocking of the central model asperity results in coseismic slip on the megathrust. The coseismic slip on the megathrust corresponds to a moment magnitude M_W=8.7, computed using the average elastic shear modulus of the overriding and subducting plates. Figure 7b shows coseismic horizontal surface displacements in the overriding plate. The displacement magnitude is highest (~11 m) and obliquely ocean directed above the ruptured asperity. Figure 7d shows a strong decrease of trench-perpendicular displacement with distance from the trench, and a change in the gradient at the mechanical contrast. Trench-parallel displacements are less affected by the contrast. However, both components are significantly non-zero beyond the compliance contrast.

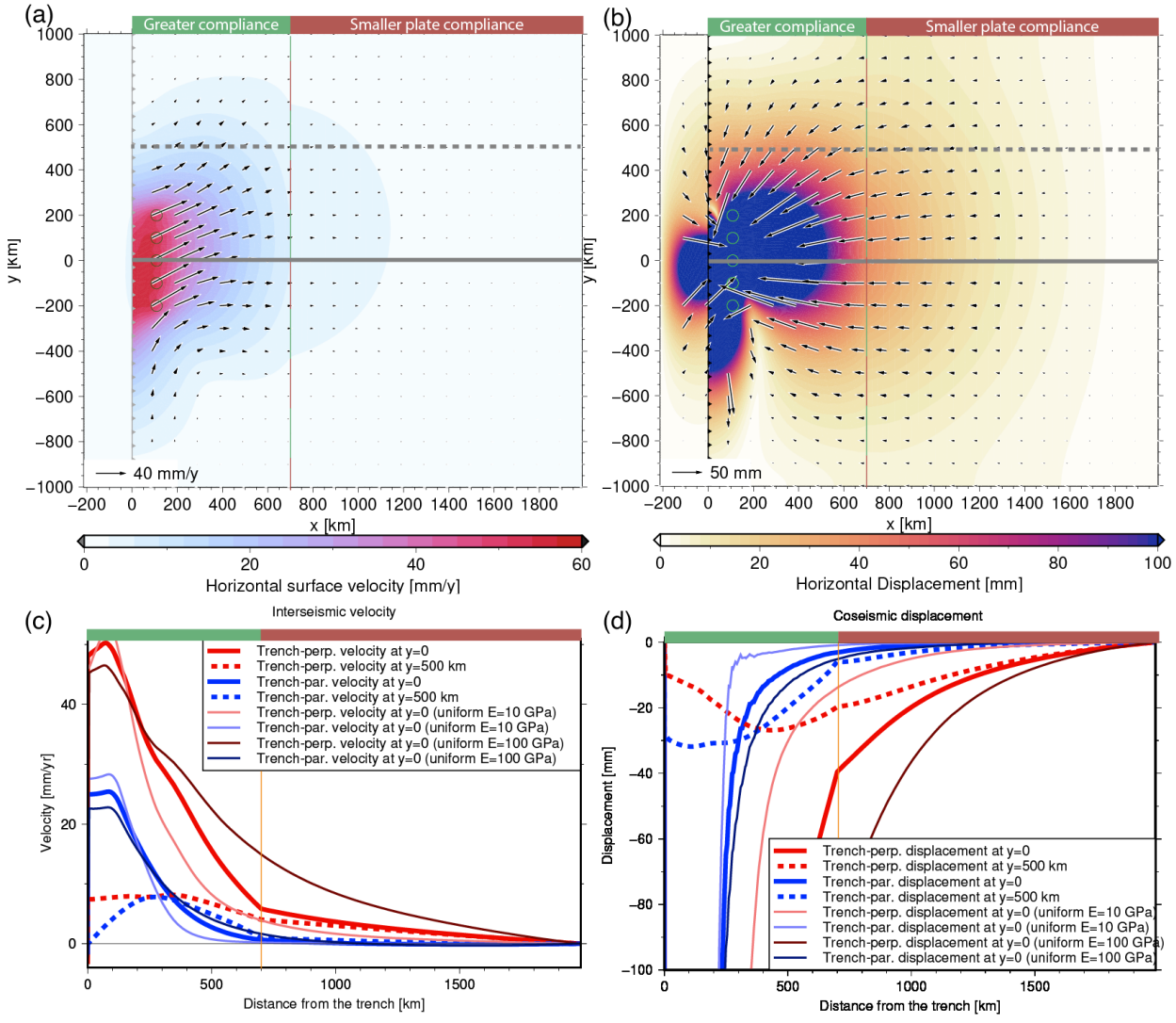

***Figure** 7. Reference model surface deformation and profiles. The extent of the forearc and backarc region with low Young's modulus E, and of the far-field region with high Young's modulus is shown above the panels. **(a)** Interseismic horizontal velocities. Colors show magnitudes, and vectors show directions and magnitudes. The black barbed line indicates the model trench that separates the subducting plate (left) from the overriding plate (right). Black circles are surface projections of locked asperities. Solid and dashed thick gray lines correspond with transect locations in panels (c) and (d). **(b)** Coseismic horizontal displacements due to unlocking of the central asperity. Colors show magnitudes, and vectors show directions and magnitudes of horizontal surface displacements. **(c)** Interseismic surface velocity components along transects on the overriding plate shown in (a) with the same line stroke (continuous or dashed). Positive velocities are landward, to the right. **(d)** Coseismic displacement components along a trench-perpendicular transects show in (b). Seaward displacement is negative, to the left.*

4.2 Lateral compliance contrast versus a homogeneous plate

We compare the results of our reference model with results from two other models, both with an overriding plate with a uniform Young's modulus, and all else the same as in the reference model (Figure 7c). We find that a low uniform value of 10 GPa produces a steep decrease in both interseismic velocity components, i.e., it concentrates interseismic strain closer to the trench. However, it lacks significant trench-perpendicular coseismic displacement in the far-field, with amplitudes below 10 mm at distances from the trench greater than 800 km, unlike our reference model. Conversely, a uniform, realistic value of 100 GPa for the overriding plate produces large far-field coseismic displacement. However, its trench-perpendicular interseismic velocities decrease slowly and have significant amplitudes (more than a third of the peak value) at the location of the contrast in the reference model (700 km from the trench).

We conclude that a uniform overriding plate cannot simultaneously explain the observed interseismic hurdle and far-field coseismic displacements. A compliance contrast in the overriding plate does explain an interseismic hurdle and far-field coseismic displacements.

4.3 Radial elasticity variations

Pollitz et al. (2011a, 2011b) concluded that radial elasticity layering is needed for fitting both the near- and far-field coseismic static GNSS displacements following the Maule and Tohoku earthquakes. We evaluate to what extent a radial elasticity variation affects the model results. We use elastic moduli varying with depth according to PREM (Dziewonski & Anderson, 1981; Pollitz et al. 2011a,b). The modeled interseismic surface velocities differ little from a model with uniform Young's modulus E=100 GPa (Figure S15), being less than 5% higher or lower and near-indistinguishable beyond 300 km of distance from the trench. We conclude that the hurdle-type response of interseismic velocities cannot be explained by the radial elasticity layering only. In the context of our numerical models a lateral contrast is thus needed in the overriding plate to reproduce the hurdle-like observations. In Sections 5.2 and 5.3 we address the tectonic and rheological viability of a mechanical contrast in overriding plates.

4.4 Importance of near-trench elasticity and of its contrast with far-field elasticity

The reference model uses a Young's modulus E=50 GPa in the near-trench and E=250 GPa in the far-field of the overriding plate. The latter value is beyond the upper limit of ~200 GPa for lithospheric rocks (specifically eclogite; Aoki and Takahashi, 2004; Christensen, 1996). Here we explore the sensitivity of our model results to elastic properties.

We systematically vary the Young's modulus in both the near-trench and the far-field portion of the overriding plate. Figure 8 shows trench-perpendicular profiles of interseismic velocities through the central asperity for models where the Young's modulus is higher in the far-field than near the trench by a factor of 5 (purple), 7.5 (red) and 10 (orange). We also vary the Young's modulus of the far-field while keeping the contrast in Young's modulus E the same (continuous, dashed, or dotted lines in Figure 8). The results show that low E-values in the near-trench region result in a sharper decrease of trench-perpendicular velocities within 700 km from the trench, and lower velocities beyond the contrast (Figure 8a). Results for the same near-trench Young's modulus show that the contrast little affects the trench-perpendicular velocities. Figure 8a shows a significant effect of the contrast in E, but that is thus driven primarily by the connected variation in near-trench Young's modulus. However, a contrast of 5 or higher is required for producing a hurdle-like response as is shown by the curve for a contrast of 1 (uniform overriding plate), which

757 does not show a hurdle. We thus take the trench-perpendicular hurdle to be a good indicator of the
758 location of a compliance contrast in the overriding plate.

759 The near-trench Young's modulus also controls the decrease in trench-parallel interseismic
760 velocities with distance from the trench, with lower values causing a steeper decrease on the
761 landward side of the peak velocity (Figure 8b). We observe however that all curves decrease to
762 low velocities at the contrast, i.e., hurdle behavior of trench-parallel interseismic velocities is not
763 a very strong indicator for a compliance contrast.

764 Figure 9 shows profiles of trench-perpendicular coseismic displacement of the same models as in
765 Figure 8. The amplitude of the displacement is controlled by the Young's modulus in the near-
766 trench, more compliant portion of the plate, regardless of the contrast with the higher Young's
767 modulus in the less compliant internal portion. A near-trench Young's modulus $E \geq 20$ GPa is
768 needed for a coseismic displacement greater than 20 mm 700 km from the trench (where the
769 contrast is located in the reference model), while a modulus of 50 GPa is needed for a displacement
770 of 20 mm 1000 km from the trench. This need for a moderate E in the near-trench region, combined
771 with the need for a sufficient E contrast in to reproduce the hurdle behavior in trench-perpendicular
772 velocities, requires the use of a very high far-field E in the overriding plate of the reference model
773 (Section 4.1) to produce realistic behavior both interseismically and coseismically. If the far-field
774 E is only moderately high (~100 GPa or less, for instance), the contrast between far-field and
775 relatively near-trench E is probably insufficient to explain hurdle behavior, given that coseismic
776 displacement requires near-trench E to be moderate. In this case, the compliance contrast within
777 the overriding plate, responsible for the hurdle, should be greater than implied by the elastic moduli
778 of the constituent materials alone. In Section 5.3 we discuss the rheological implications of the
779 model sensitivities presented here.

780

781 *4.5 Shear modulus contrast in the overriding plate*

782 We thus far focused on contrasts in Young's modulus E, which is the resistance to interseismic
783 (elastic) shortening of the overriding plate in response to the head-on component of the
784 convergence velocity. The resistance to (elastic) shear deformation due to the trench-parallel
785 component of the convergence velocity is better represented by the shear modulus $G = \frac{E}{2(1+\nu)}$.

All presented models used a uniform Poisson's ratio ν=0.25, meaning that the contrasts in Young's modulus E and shear modulus G are the same. We now test whether varying the contrast in G while keeping the contrast in E constant, affects trench-perpendicular and -parallel velocities. The near-field and far-field values of E are 30 and 150 GPa, respectively, while ν is 0.2. We decrease the near-field G by 14% through a drastic increase (doubling) in Poisson's ratio, to 0.4, which results in a slight change in the trench-parallel velocity, but does not alter the trench-perpendicular velocity (Figure S16). Different contrasts in E and G are thus unlikely to affect the apparent hurdle location, particularly as determined in the trench-perpendicular component of velocities, justifying our use of the same contrast in both moduli.

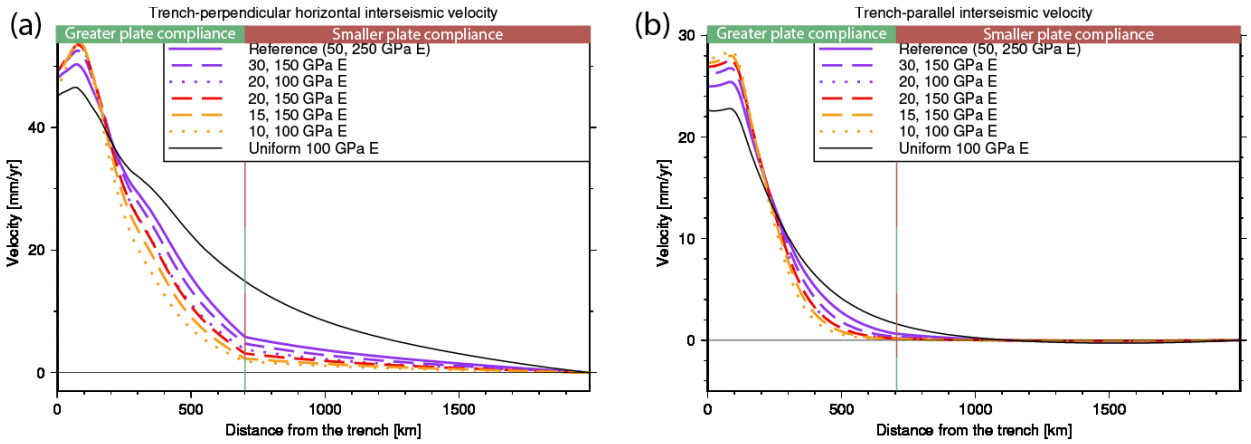

Figure 8. *Interseismic velocity components along the transect through the central asperity (solid grey line in Fig.7a). The extent of the forearc and backarc region with low Young's modulus E, and of the far-field region with higher Young's modulus is shown above the panels.* ***(a)*** *Trench-perpendicular velocity, and* ***(b)*** *and trench-parallel velocity. Colors correspond with models with a given ratio of the far-field and near-trench Young's moduli. Dashed and dotted lines represent models with different average Young's modulus.*

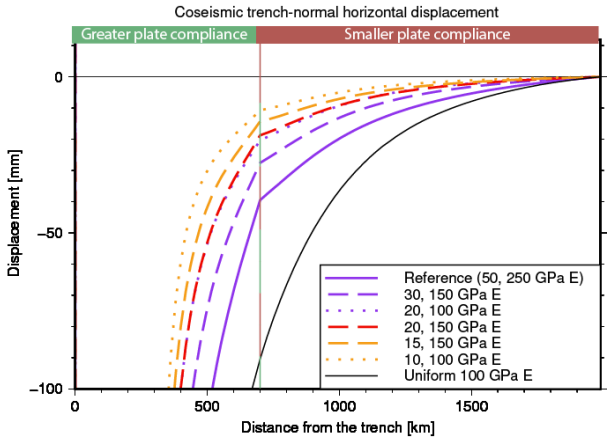

804

805 **Figure 9**. Trench-perpendicular profiles of intermediate- and far-field trench-perpendicular
806 coseismic displacement at y=0, for models with different contrasts in E and for a uniform model
807 as comparison. Colors identify different ratios of the two values of E, while dashed and dotted
808 lines identify increasingly lower mean E in the overriding plate. The value of E on the trenchward
809 side of the contrast controls the far-field coseismic displacement.

810

811 *4.6 Role of the location of the mechanical contrast*

812 We investigate the sensitivity of the models to the location of the contrast in E by stepwise
813 reducing its distance from the trench to 400 km in 100 km intervals. We do so in a model with a
814 contrast that produces the largest differences in interseismic velocities compared to a uniform E
815 (10 and 100 GPa; Figure 8). Bringing the contrast closer to the trench most noticeably affects
816 trench-perpendicular velocity profiles (Figure 10a). Increasing the contrast distance produces less
817 uniform decay of such velocities on the trenchward side of the contrast, as the slope becomes
818 shallower before reaching the contrast. Instead, when the contrast distance is increased, the
819 velocities at the contrast become lower while beyond the contrast, the slopes become flatter.
820 Trench-parallel velocities are much less affected by the location of the contrast (Figure 10b), as
821 the near-trench value of E controls the general shape of the decrease. The presence of a single
822 contrast in E can thus produce a varying distance between the apparent location of the hurdle (a
823 sharp transition between a steep decay and near-0 amplitudes) in the two components of horizontal
824 interseismic velocities, depending on the near-trench value of E and its spatial extent. Overall, the
825 two horizontal velocity components not only have different spatial distribution with the same
826 contrast, but also respond differently to variations in distance to the contrast or in the value of E

on either side of the contrast. This behavior is compatible with our observations showing that the apparent location of the trench-parallel hurdle relative to the trench-perpendicular one varies along a subduction zone and between subduction zones, rather than coinciding with it or being offset by a constant distance.

Interseismic locking results in steadily increasing shear tractions on asperities. The slope of the velocity curves in Figure 10 represents horizontal strain accumulation rates in the overriding plate. In the region within 200 km from the trench, strain accumulation rates show to be insensitive to the distance of the contrast, and shear tractions on asperities are consequently expected to be insensitive to the width of the zone where strain accumulates. Figure S15 shows indeed that the average traction on the middle asperity in the downdip direction increases little with decreasing trench-contrast distance; for instance, the traction becomes only ~3% larger when the distance to the contrast reduces from 700 to 500 km. The temporal rate of change of this traction at the end of the cycle in the late interseismic phase is linear and thus increases by the same, small amount. Overall, the presence and location of the mechanical contrast in the overriding plate has little effect on stressing rates on locked asperities.

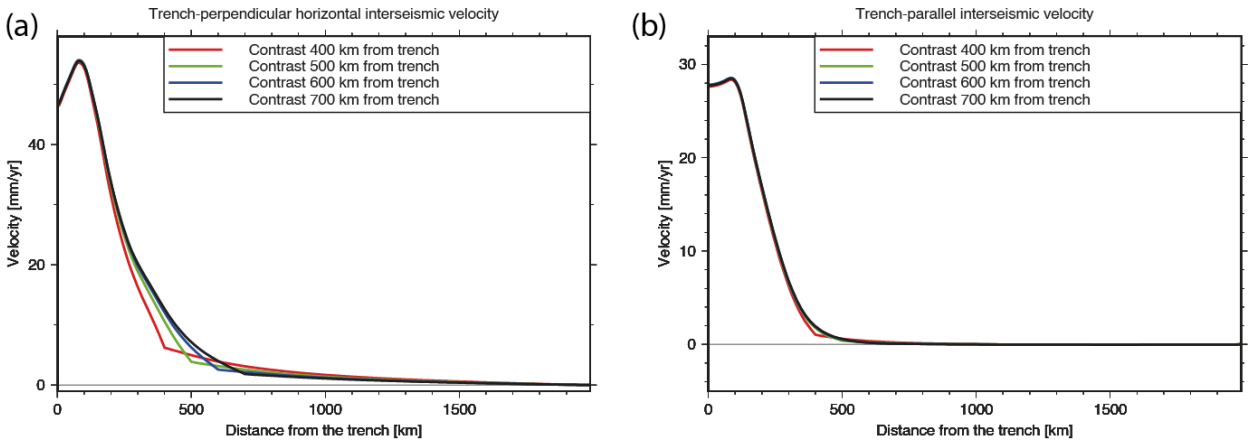

Figure 10. *Trench-perpendicular profiles through the middle of the model, at y=0, of the interseismic horizontal surface velocity components, trench-perpendicular (a) and trench-parallel (b), respectively, for models with a contrast in the E value of the overriding plate (10 GPa near-trench, 100 GPa in the far-field) for different trench-contrast distances.*

849 *4.7 Megathrust locking pattern affects the detectability of hurdles and contrasts*

850 To assess the effect of a contrast on interseismic velocities in areas of low interplate locking, such
851 as northern Peru and Ecuador (Herman & Govers, 2020; Nocquet et al., 2017), we run two
852 simulations in which the two intermediate asperities are removed, leaving 3 total asperities (2
853 lateral asperities centered 200 km from the center of the middle one). We cut a profile halfway
854 between the middle and outer asperities (at y=100 km) (Figure 11). The profile through the former
855 asperity (with 3 remaining asperities in the model) has lower trench-perpendicular velocities than
856 the same profile through the asperity (model with 5 asperities), with a shallower slope of decrease
857 in the near-trench portion of the overriding plate, but still with a clear hurdle in the form of a break
858 in the slope at the location of the contrast in E (Figure 11a). Trench-parallel velocities have a
859 similar behavior, except that velocities beyond the contrast are approximately identical.

860

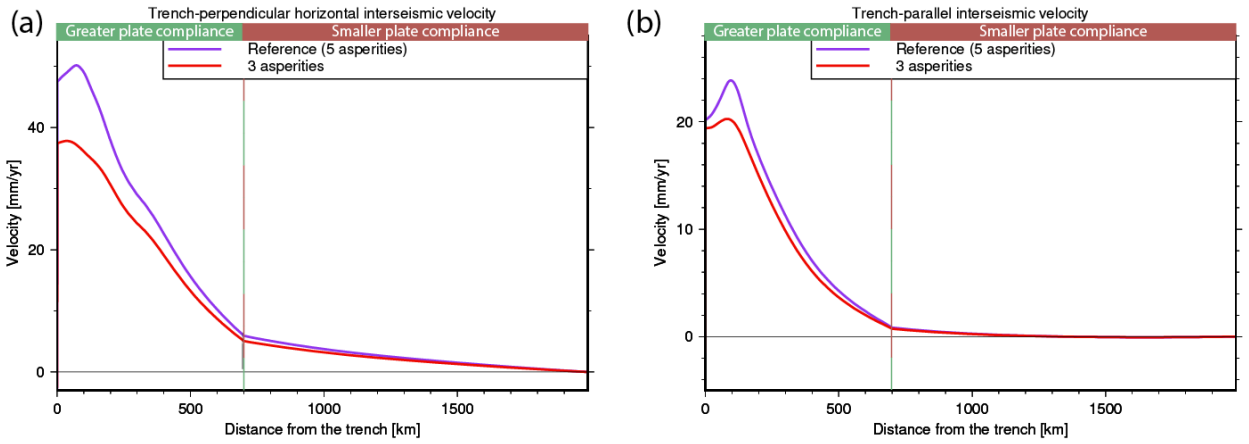

861

862 ***Figure 11***. *Trench-perpendicular profiles at y=100 km (through the middle of one of the*
863 *intermediate asperities, if present) of the two horizontal velocity components, trench-*
864 *perpendicular (a) and trench-parallel (b), of interseismic velocities in a model with or without an*
865 *intermediate asperity centered at y=±100 km, halfway between the middle one (at y=0) and each*
866 *of the outer ones (at y=±200 km).*

867

868 *4.8 Lateral thickness variation and sharpness of the mechanical contrast*

869 In our models, a contrast in elastic moduli in an overriding plate of uniform thickness is a proxy
870 for a general contrast in the plate's elastic compliance. We test the addition of a step increase in

overriding plate thickness, doubling in thickness from 40 km at x<700 km to 80 km at x≥700 km, to our reference model and to the model with a uniform E of 100 GPa. The trench-perpendicular interseismic velocity decreases ~30% at the contrast while leaving the peak value unaffected, thus making its decrease with distance from the trench slightly steeper on the oceanward side of the contrast and more gradual on the beyond the contrast (Figure 12). Trench-parallel velocities are unaffected by the thickness contrast. Heterogeneity in overriding plate thickness, and particularly a thinner arc region, likely contributes to the observed behavior of interseismic surface velocities, but is not solely responsible for hurdle characteristics.

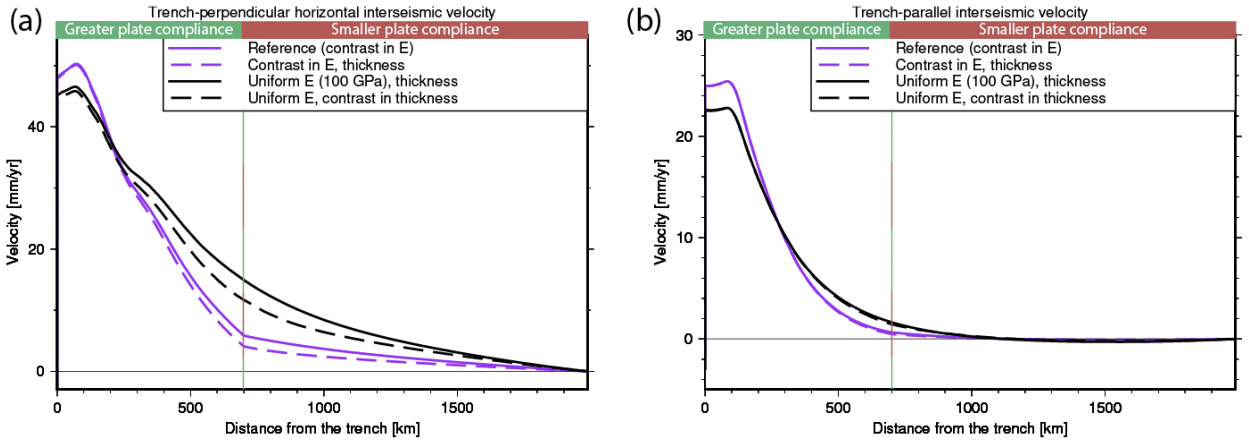

Figure 12. *Trench-perpendicular profiles at y=0 km of the two horizontal components, trench-perpendicular (a) and trench-parallel (b), of interseismic velocities in a model with or without a contrast in overriding plate thickness (40 km at x<700 km, 80 km at x>700 km). In both models there is the same contrast in overriding plate elastic moduli: the thinner portion of the plate has E=50 GPa and the thicker one E=250 GPa.*

4.9 Effect of the ratio of the earthquake recurrence interval to the Maxwell time

The ratio $\frac{T}{\tau}$ of the earthquake recurrence interval T to the characteristic Maxwell relaxation time $\tau = \frac{\eta}{G}$ is an important property of the megathrust system. In fact, it determines to what extent coseismic stresses have relaxed late in the cycle, and thus to what extent late interseismic motion reflects steady-state loading of the plate due to continued convergence and locking (Savage, 1983). Our models so far use a $\frac{T}{\tau}$ ratio of 37.9, intermediate for the range of possible ratios observed for subduction zones worldwide and representing a case in which the stress changes due to coseismic

slip and afterslip have relaxed late in the cycle (Govers et al., 2018a). We now explore the effect of reducing the $\frac{T}{\tau}$ ratio of the model with uniform elastic moduli throughout (ν=0.25, E=100 GPa in the overriding plate and elsewhere), while keeping the convergence rate and earthquake size constant. Figure 13 shows the interseismic velocity profiles for the model with the reference model viscosity of 10^{19} Pa·s (black line, same model and curves as in Figs. 7, 8, and 11), and for alternative models with higher viscosities (i.e., longer relaxation times and smaller $\frac{T}{\tau}$) of the viscoelastic mantle. The resulting interseismic model velocities decrease more steeply with distance from the trench with decreasing $\frac{T}{\tau}$. The effect is particularly significant for the trench-perpendicular component, which decreases quite gradually for $\frac{T}{\tau}$=37.9. When the $\frac{T}{\tau}$ ratio is halved to 18.9, the effect is limited and the trench-perpendicular velocities still decrease shallowly with distance. However, further reducing $\frac{T}{\tau}$ makes the slope at intermediate-field distances even steeper, and particularly $\frac{T}{\tau}$ <10 makes the velocity 700 km away from the trench equal to or lower than 25% of the peak value. This indicates that, for a sufficiently long Maxwell time relative to the earthquake recurrence interval, the hurdle behavior exhibited by observed trench-perpendicular velocities may be explained without invoking a contrast in the compliance of the overriding plate. We further discuss the viability and implications of such explanation in Section 5.2.

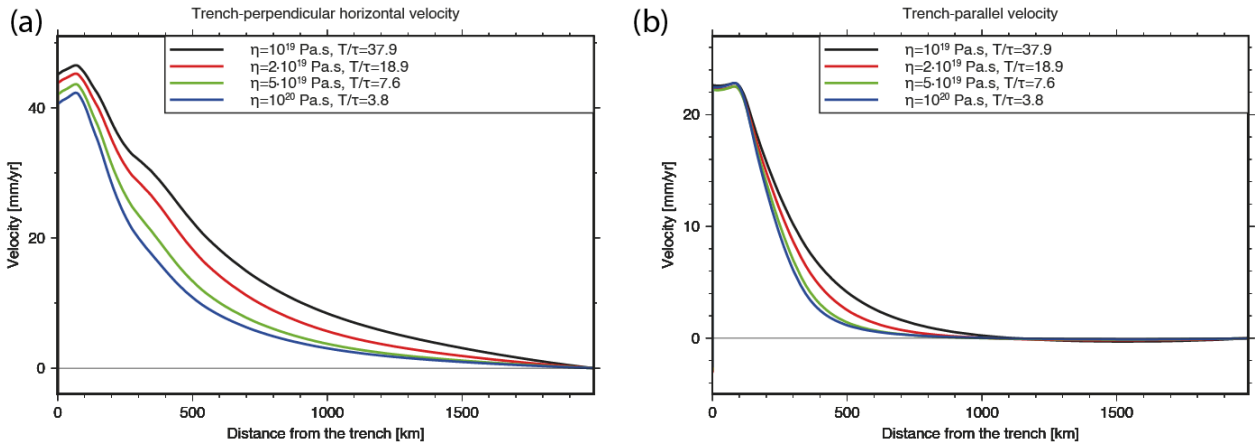

Figure 13. *Trench-perpendicular profiles at y=0 km of the two horizontal components, trench-perpendicular (a) and trench-parallel (b), of interseismic velocities in models with a uniform E of 100 GPa and different values of viscosity* η, *and thus Maxwell characteristic relaxation time* τ *and the ratio* $\frac{T}{\tau}$ *of the earthquake return period T to* τ, *in the viscoelastic mantle domains.*

5 Discussion and implications

5.1 Scope and limitations of our study

We reevaluate published interseismic GNSS velocity observations along three subduction margins: the Peru-Chile Trench (South America), the Sunda Trench (Sumatra, Java), and the Japan Trench (Hokkaido and northern Honshu). In South America, our analysis is not hampered by marine basins, which therefore yields the most continuous sampling of the kinematics in the overriding plate. The analysis will need to be extended to other convergent margins before we can conclude that hurdles, breaks in the interseismic velocity gradient, are global features of megathrust margins. Still, with three out of the three margins showing hurdles, we think that we have a basis to hypothesize a more common feature that mechanically separates the deforming margin from a semi-stable overriding plate interior.

Our mechanical models are generic in their geometry, earthquake cycle, and mechanical properties. Further work will be needed to model the specific contribution of regional rheological makeup and active deformation structures to interseismic velocities. It will be important to also include radial elasticity variations and the sphericity of the Earth. The former feature decreases near-trench velocities, and far-field velocities remain the same (Pollitz et al., 2011b, 2011a; see also Section 4.3). Sphericity has been shown by Nostro et al. (1999) to have a negligible effect on coseismic horizontal displacement due to thrust faulting at distances of 0 to 5000 km from the trench. Trubienko et al. (2013) showed that interseismic displacement normalized by coseismic displacement 700 km from the trench has the same slope towards the end of the cycle, regardless of sphericity, indicating that interseismic velocities at the end of the cycle should also be hardly affected.

5.2 Role of the Maxwell time in relation to the earthquake recurrence interval

As we show in Section 4.9, low values (broadly below 10) of the $\frac{T}{\tau}$ ratio cause the velocities to decrease more steeply with distance from the trench. Coseismic stresses have not fully relaxed before the next earthquake occurs, and as a result viscoelastic model results become similar to those of fully elastic models. This effect is consistent with the results of earthquake cycle models of Li et al. (2015) and Trubienko et al. (2013). Trubienko et al. (2013) explain the spatial

distribution of interseismic velocities in a transect through central Sumatra and the Malay peninsula, as well as one in northern Honshu in Japan, using an earthquake cycle model with a uniform elastic overriding plate. Their model employs a plane-strain approximation, a Burgers viscoelastic rheology for the mantle with a steady-state (Maxwell) viscosity $\eta = 3 \cdot 10^{19}$ Pa·s, asthenospheric elastic parameters from PREM (Dziewonski and Anderson, 1981; giving $G \approxeq 68$ GPa and $\nu \approxeq 0.28$ in the asthenosphere), and a return period of 170 years. Their $\frac{T}{\tau}$ is thus ~7.2, accounting for the fact that τ is $3\frac{1-\nu}{1+\nu}\frac{\eta}{G}$ higher in the plane strain regime (Melosh and Raefsky, 1983). Li et al. (2015) similarly reproduce interseismic velocities in the North Chile portion of the Andean subduction zone in a model with a uniform overriding plate, a viscosity of $4 \cdot 10^{19}$ Pa·s in the Maxwell viscoelastic mantle underlying the overriding plate, an earthquake cycle duration of 200 years, and a resulting $\frac{T}{\tau}$ of ~10.1.

Li et al. (2015) and Trubienko et al. (2013) do not incorporate finite gradients in slip deficit downdip of the locked interface and instead impose slip deficit to sharply transition from non-zero to zero at the downdip end of the megathrust. A sharp transition in slip deficit is physically unlikely (Herman and Govers, 2020) and precludes the occurrence of the intermediate-depth afterslip (down to at least 80 km depth) that has been inferred from geodetic and seismological observations (Diao et al., 2014; Freed et al., 2017; Hu et al., 2016; Sun et al., 2014; Yamagiwa et al., 2015). The depth to which slip deficit accumulates is especially important, as Li et al. (2015) and Trubienko et al. (2013) show that greater locking depths producing larger intermediate- and far-field velocities. These studies rely on shallow locking depths to reproduce interseismic velocities. Furthermore, when inverting observations, Li et al. (2015) do not apply a model spin-up, necessary to obtain viscous stresses and strain rates consistent with the long-term repetition of the earthquake cycle. As Li et al. (2015) point out, the spin-up would increase horizontal velocities, particularly in the intermediate-field (100–300 km from the trench), decreasing their trench-perpendicular slope. Therefore, the steepness of the decrease in interseismic velocities with distance from the trench is overestimated for a given $\frac{T}{\tau}$ ratio in the models of Li et al.(2015) and Trubienko et al. (2013). Nevertheless, their results suggest that low $\frac{T}{\tau}$ ratios might explain the apparent hurdle behavior of interseismic velocities in the absence of contrasts in the compliance of the overriding plate.

Models of postseismic relaxation following the 2004 Sumatra-Andaman earthquake, using Burgers rheologies for the asthenospheric mantle, consistently indicate steady-state viscosities of ~10^{19} Pa·s, corresponding to a Maxwell time τ of ~5 years (Govers et al., 2018a; Hu and Wang, 2012; Qiu et al., 2018), while the recurrence interval for an earthquake of similar size has been estimated to be between 174 and 600 years (Gahalaut et al., 2008; Meltzner et al., 2010; Van Veen et al., 2014), yielding $\frac{T}{\tau}$ ratios of 34.8–120. For the Chilean convergent margin, Klein et al. (2016) and Li et al. (2018) invert postseismic GNSS observations in the few years (5 and 8, respectively) following the 2010 Maule earthquake, using a Burgers or Maxwell viscoelastic rheology, and consistently find Maxwell viscosities of 5–6·10^{18} Pa·s in the continental asthenosphere under the Andes, corresponding to Maxwell times of 2.4–3.0 years. Aron et al. (2015) estimate the return period as within a range of 84–178 years range, which would put $\frac{T}{\tau}$ in the 28.0–74.2 range. In the Japan subduction zone, simultaneous inversions of GNSS time series following the 2011 Tohoku earthquake into afterslip and visco-elastic relaxation parameters, using Burgers or non-linear flow law–based visco-elastic rheologies for the asthenosphere, indicate that the steady-state viscosity of the mantle wedge is in the range of $4 - 10 \cdot 10^{18}$ Pa·s (Agata et al., 2019; Fukuda and Johnson, 2021; Muto et al., 2019). This corresponds to Maxwell relaxation times of 2.0–5.0 years and is in agreement with the results of the inversion of gravity data into viscous relaxation parameters only by Cambiotti (2020). The recurrence interval T for events similar to the 2011 Tohoku-oki earthquake is ~600 years (Satake, 2015), which puts the $\frac{T}{\tau}$ ratio in the 120–300 range. The ratios (12.1 and 7.2, respectively) used by Trubienko et al. (2013) and Li et al. (2015) are thus below the low end of the realistic range. Our models reproduce the hurdle-like response for low ratios of $\frac{T}{\tau}$ (section 4.9). Higher ratios are more realistic for the active margins that we investigate, and our model results show that hurdle behavior is not reproduced with high $\frac{T}{\tau}$ ratios (mantle viscosities in line with the majority of postseismic studies) combined with uniform elastic compliancy of the overriding plate (sections 4.2 and 4.4). This argues for compliancy contrasts in the overriding plate.

5.3 Tectonic significance of a mechanical contrast

Klein et al. (2016) suggest that stiff cratonic back-arc lithosphere in central Argentina affects horizontal and vertical postseismic surface velocities following the Maule earthquake. Li et al.

(2018) invert postseismic displacements, including in the far field, following the Maule earthquake into rheological structures of the upper mantle, finding strong evidence for a strong (elastic, or viscoelastic with high viscosity) cratonic lithospheric root beneath central Argentina. Seismic data also indicate that the Andean lithosphere has very thick crust and warm lithospheric mantle that contrast with thinner (but still thick) cratonic crust underlain by cold, stiff lithospheric mantle farther to the east, from Venezuela to central Argentina (Chulick et al., 2013). This juxtaposition represents a significant contrast in lithospheric averages of the compliance. The hurdle location that we inferred from the GNSS velocities agrees with the tectonic boundary (Section 2.5, Figure 5a). Immediately to the south of the Central Andes, around 30°S, the trench-perpendicular hurdle coincides with different terrane and active tectonic boundaries (Figure 5a; Ramos, 1999, 1988). In particular, it is located between the eastern front of the active Andean Precordillera fold-and-thrust belt (Baldis et al., 1982; Ortiz & Zambrano, 1981) and the western margin of the Rio de la Plata craton (Álvarez et al., 2012), within a mountain range (the Sierras Pampeanas) characterized by active reverse faults and lateral contrasts in crustal thickness and layering (Perarnau et al., 2012) (Figure 5a). The western edge of the Andes as marked by active faults correlates spatially with the western edge of the distinct, stable, largely cratonic interior of the South America plate. Thus, the general but imperfect coincidence of the hurdle with the active backthrust, where present, is consistent with the hurdle being determined by a contrast in compliance that occurs with different amplitudes and different depth dependences along the orogen.

In Sunda, the overriding plate is a set of Paleozoic-Cenozoic accreted terranes (Hall et al., 2009). We are unaware of independent proof that Sundaland is mechanically stronger than the Sumatra forearc. However, a significant crustal contrast exists across the Meratus paleosuture in Java (Figure 5b; Haberland et al., 2014). Contrasts may also exist across two major structural boundaries. The first of these is peninsular Malaysia's Bentong-Raub suture zone, which separates the Sibumasu terrane to its southwest from the Indochina terrane (Metcalfe, 2000). The second boundary is the Medial Sumatra Tectonic Zone, which separates the Sibumasu terrane to the northeast from the West Sumatra block and the overlying Woyla accretionary complex and volcanic arc (Barber, 2000; Barber et al., 2005; Hutchison, 2014, 1994) and which largely coincides with the strike-slip Sumatran Fault in central and northern Sumatra. Simons et al. (2007) used GNSS data to identify the approximate boundaries of the interseismically nondeforming part of the Sundaland block (Michel et al., 2001); its internal (south and west) boundary aligns roughly

with geological suture boundaries. On the other hand, estimates from coherence between gravity and topography show no evidence of a block in the interior of the plate with higher T_e than the forearc region (Audet & Bürgmann, 2011; Shi et al., 2017).

To explain the steep spatial gradient near the trench in horizontal interseismic velocities in Hokkaido, Japan, Itoh et al. (2019, 2021) proposed and modeled the effect of a compliant (less stiff or thinner) lithosphere in the volcanic arc and back-arc, in contrast with a less compliant (thicker) forearc, as evidenced by temperature, heat flux, and seismic wave attenuation (Katsumata et al., 2006; Kita et al., 2014; Liu et al., 2013; Tanaka et al., 2004; Wada & Wang, 2009; Wang & Zhao, 2005). However, in the model of Itoh et al. (2019) velocities are restricted by the fixed landward edge of the domain, which localizes shortening and shearing in the compliant material. We propose that velocities are instead restricted by the contrast between the compliant arc and back-arc and the stronger material farther from the trench, in the Sea of Japan and beyond. The Sea of Japan is a Miocene back-arc basin of the Japan and southern Kurile subduction zones. It is inactive (Karig, 1974), having ceased extending around 14 Mya (Tatsumi et al., 1989), and is likely less compliant than the Japan arc. The Amurian-Okhotsk plate boundary follows the sea's eastern margin (Seno et al., 1996) (Figure 5c), hosts Mw 7.6-7.8 thrust earthquakes (Satake, 1986; Sato et al., 1986; Tanioka et al., 1995) and accommodates a relative velocity of 9-17 mm/yr (Jin et al., 2007). The plate boundary mechanically decouples these plates in the long term, but they are coupled during most of the earthquake cycle. The lack of GNSS observations in the Sea of Japan prevents us from determining where exactly the compliance contrast occurs and whether creep along the plate boundary further affects velocities.

5.4 Compliance contrasts in a rheological and geodynamic context

As stated in Section 4.4, our model results suggest that interseismic velocities necessitate a larger contrast in interseismic compliance within the overriding plate than can be provided by realistic elastic parameters. In fact, the Young's modulus needs to be high enough in the portion of the plate between the trench and the hurdle as to transmit substantial coseismic displacement to the far-field, and low enough in the far-field interior of the plate as to not exceed plausible values. The portion of the plate between the trench and hurdle must thus transition from its coseismic compliance, dictated by elastic properties, to greater compliance in the interseismic period. This transition

might be related to viscous creep of the lower crust and upper mantle (Bürgmann & Dresen, 2008), which reduces flexural rigidity (Ranalli, 1995), and likely also compliance, over time after loading. Low effective elastic thickness is thought to indicate departure from purely elastic rheology, such as due to high temperatures, inherited weak zones, or high horizontal stresses (Burov & Diament, 1995), which are likely to occur in the thermomechanically young lithosphere at convergent boundaries. The increased water content at subduction zones also contributes to departure from elasticity by weakening the lower crust and upper mantle, in terms of both lower viscosity (Chopra and Paterson, 1984; Hirth and Kohlstedt, 1996; Kirby, 1983) and lower plastic strength (Blacic and Christie, 1984; Mainprice and Paterson, 1984). Geodynamical, petrological–thermomechanical numerical modeling of subduction shows that brittle-plastic rheological weakening by both fluids and melts plays an important role in the evolution of the subduction zone and in the development of the volcanic arc and the back-arc region (Gerya & Meilick, 2011).

5.5 Geodetically stable parts of overriding plates?

Observations of significant coseismic displacements thousands of km away from the megathrust rupture called into question the concept of an undeforming (rigid) reference plate (Pollitz et al., 2011a; Vigny et al., 2005; Wang et al., 2011; see also Section 4.1). Our analysis shows indeed that small but significant interseismic velocity gradients extend well beyond hurdles, and this presents a challenge for defining a reference on a geodetic observation time scale. On time scales spanning the time needed to complete a seismic catalog on the megathrust (tens to thousands of years, e.g., Ward 1998), it is possible that the net accumulated strain is zero, i.e., there may exist a fully rigid reference on geological time scales.

5.6 Role of major faults in the Central Andes

As discussed in Section 2.6, previous studies observe and explain the spatial behavior of interseismic velocities, in the context of the Central Andes, as a result of shortening on back-thrusts (Bevis et al., 2001; Brooks et al., 2011a, 2003a; Kendrick et al., 2006; McFarland et al., 2017a; Norabuena et al., 1998; Shi et al., 2020; Weiss et al., 2016a). Quantitative models in these studies use either a uniform elastic half-space, or apply zero-displacement boundary conditions close to the back-thrust. Both model types artificially restrict interseismic velocities to the near-trench

region, compared to models with elastic plates overlying viscoelastic mantle and extending well into the far-field. To explain the observed interseismic surface velocities, most of the studies also need basal thrusts that are more spatially extensive than supported by geological evidence (see Section 2.6). However, more localized shortening, particularly in back-arc thrust belts and basal faults as well as thrusts in the interior of orogens at the active margin, have a more regional role in determining specific trench-perpendicular velocities. For instance, locally they may cause discontinuities and increased spatial gradients, without affecting the near-trench portion of the velocity field (Shi et al., 2020). Major, creeping strike-slip faults likely cause large local gradients in trench-parallel velocities, and can localize trench-parallel velocities in a way not necessarily related to the presence of a contrast (Section 2.6). Nevertheless, contrasts in lithologies and plate thickness, responsible for hurdles, might also result from continued motion along strike-slip faults. In turn, the presence of such contrasts might localize lateral motion into narrow fault zones.

6 Conclusions

Interseismic GNSS velocities from the three studied subduction zones show a broadly linear decrease of the trench-perpendicular velocity with distance from the trench up to what we define as the hurdle, located at variable distances less than 1000 km. Beyond the hurdle, trench-perpendicular velocities are near-zero (less than ~5 mm/yr) extending over thousands of kilometers away from the trench. Trench-parallel velocities are in some cases affected by presence of strike-slip faults (Sumatra), or are insignificant because of head-on convergence (Japan, Java). In South America, however, they generally also decrease steeply with distance, up to a hurdle. The hurdle roughly coincides with the trench-perpendicular hurdle or is located up to several tens of km closer to the trench. This interseismic deformation restricted to the near-trench region contrasts with significant coseismic displacements that were recorded beyond these hurdles during the large 2004 Sumatra, 2010 Maule and 2011 Tohoku earthquakes.

The location of the hurdle in observed trench-perpendicular velocities often coincides with major tectonic or geological boundaries separating a plate margin region from a distinct, and likely more rigid, plate interior. In South America the trench-perpendicular hurdle generally follows the eastern edge of the orogen, coinciding with the western margin of the cratonic lithosphere and the eastern margin of the accreted, deformed terranes at the active plate margin. In Sumatra, the hurdle follows the Medial Sumatra Tectonic Zone. Off the shore of northern Honshu and Hokkaido in

Japan, the hurdle probably coincides with the boundary between the back-arc region of the islands, to the east, and the inactive back-arc basin and Amur plate interior to the west.

Our numerical modeling results show that a contrast in overriding plate compliance can reproduce the steep, largely linear near-trench decrease in trench-perpendicular velocities. In our models, this decrease ends abruptly at the location of the contrast, i.e., at the hurdle. The value of elastic moduli on either side of the contrast contributes to the intensity hurdle behavior: a lower value near-trench or a higher value in the far-field steepens the near-trench trench-perpendicular gradient. Trench-parallel velocities are instead controlled by the near-trench elastic moduli and decrease more gradually. The steep decrease in the first couple of hundred km from the trench defines an apparent hurdle that, for the values tested in our models, is closer to the trench than the location of the contrast. The distance between the two depends on the specific elastic moduli and the location of their contrast.

The presence and location of compliance contrasts does not significantly affect the rate at which shear traction increases on the asperities in our models. The width of the zone where interseismic strain primarily accumulates, roughly between the coastline and the hurdle, likely does not generate significant variations in megathrust earthquake magnitude or recurrence interval. Velocities in portions of the subduction zone with little slip deficit, i.e., little apparent interplate coupling on the megathrust, have lower near-trench trench-perpendicular gradients but otherwise similar behavior, particularly in the trench-perpendicular components. Their near-trench trench-parallel components exhibit more complex gradients depending on location with respect to the fully coupled asperities and the direction of trench-parallel, far-field interplate motion.

Acknowledgments, Samples, and Data

We thank the following people for providing additional background information for the velocity data sets that we have used in this study: Laura Sánchez, Jean-Mathieu Nocquet, Corné Kreemer and Achraf Koulali. Insightful reviews by Emilie Klein and an anonymous reviewer contributed significantly to the improvement of an earlier version of the manuscript.

Author contributions following the CRediT taxonomy: Conceptualization: R. Govers, T. Broerse, M. D'Acquisto. Methodology: T. Broerse, M. D'Acquisto. Software: R. Govers, T.

Broerse. Validation: T. Broerse, M. D'Acquisto. Formal Analysis: M. D'Acquisto, T. Broerse. Investigation: M. D'Acquisto, C. P. Marsman. Resources: R. Govers. Data Curation: M. D'Acquisto. Writing-Original Draft: M. D'Acquisto, R. Govers, T. Broerse , C. P. Marsman. Writing-Review & Editing: M. D'Acquisto, T. Broerse, R. Govers, C. P. Marsman. Visualization: M. D'Acquisto, T. Broerse. Supervision: R. Govers. Project Administration: R. Govers. Funding Acquisition: R. Govers.

The mesh generator program Gmsh (Geuzaine and Remacle, 2009) was used to make the finite element meshes for the numerical models. The MATLAB software platform (MATLAB, 2018), the Generic Mapping Tools (Wessel et al., 2019), and the Adobe Illustrator program (Adobe Inc., 2019) were used for visualization.

Input and output files that we used for the models of this paper are digitally stored in the Yoda repository of Utrecht University and will be accessible before the end of the peer review process, in compliance with FAIR (Findable, Accessible, Interoperable, Reusable) principles.

References

Adobe Inc., 2019. Adobe Illustrator.

Agata, R., Barbot, S.D., Fujita, K., Hyodo, M., Iinuma, T., Nakata, R., Ichimura, T., Hori, T., 2019. Rapid mantle flow with power-law creep explains deformation after the 2011 Tohoku mega-quake. Nat Commun 10, 1–11. https://doi.org/10.1038/s41467-019-08984-7

Altamimi, Z., Collilieux, X., Métivier, L., 2011. ITRF2008: an improved solution of the international terrestrial reference frame. J Geod 85, 457–473. https://doi.org/10.1007/s00190-011-0444-4

Altamimi, Z., Métivier, L., Collilieux, X., 2012a. ITRF2008 plate motion model: ITRF2008 PLATE MOTION MODEL. J. Geophys. Res. 117, n/a-n/a. https://doi.org/10.1029/2011JB008930

Altamimi, Z., Métivier, L., Collilieux, X., 2012b. ITRF2008 plate motion model: ITRF2008 PLATE MOTION MODEL. J. Geophys. Res. 117, n/a-n/a. https://doi.org/10.1029/2011JB008930

1179 Alvarado, A., Audin, L., Nocquet, J.M., Jaillard, E., Mothes, P., Jarrín, P., Segovia, M.,
1180 Rolandone, F., Cisneros, D., 2016. Partitioning of oblique convergence in the Northern
1181 Andes subduction zone: Migration history and the present-day boundary of the North
1182 Andean Sliver in Ecuador. Tectonics 35, 1048–1065.
1183 https://doi.org/10.1002/2016TC004117
1184 Alvarado, A., Audin, L., Nocquet, J.M., Lagreulet, S., Segovia, M., Font, Y., Lamarque, G.,
1185 Yepes, H., Mothes, P., Rolandone, F., Jarrín, P., Quidelleur, X., 2014a. Active tectonics in
1186 Quito, Ecuador, assessed by geomorphological studies, GPS data, and crustal seismicity.
1187 Tectonics 33, 67–83. https://doi.org/10.1002/2012TC003224
1188 Alvarado, A., Audin, L., Nocquet, J.M., Lagreulet, S., Segovia, M., Font, Y., Lamarque, G.,
1189 Yepes, H., Mothes, P., Rolandone, F., Jarrín, P., Quidelleur, X., 2014b. Active tectonics in
1190 Quito, Ecuador, assessed by geomorphological studies, GPS data, and crustal seismicity.
1191 Tectonics 33, 67–83. https://doi.org/10.1002/2012TC003224
1192 Alvarado, P., Ramos, V.A., 2011. Earthquake deformation in the northwestern Sierras
1193 Pampeanas of Argentina based on seismic waveform modelling. Journal of Geodynamics
1194 51, 205–218. https://doi.org/10.1016/j.jog.2010.08.002
1195 Álvarez, O., Gimenez, M., Braitenberg, C., Folguera, A., 2012. GOCE satellite derived gravity
1196 and gravity gradient corrected for topographic effect in the South Central Andes region.
1197 Geophysical Journal International 190, 941–959. https://doi.org/10.1111/j.1365-
1198 246X.2012.05556.x
1199 Aoki, I., Takahashi, E., 2004. Density of MORB eclogite in the upper mantle. Physics of the
1200 Earth and Planetary Interiors, New Developments in High-Pressure Mineral Physics and
1201 Applications to the Earth's Interior 143–144, 129–143.
1202 https://doi.org/10.1016/j.pepi.2003.10.007
1203 Apel, E.V., Bürgmann, R., Steblov, G., Vasilenko, N., King, R., Prytkov, A., 2006a. Independent
1204 active microplate tectonics of northeast Asia from GPS velocities and block modeling.
1205 Geophys. Res. Lett. 33, 2006GL026077. https://doi.org/10.1029/2006GL026077
1206 Apel, E.V., Bürgmann, R., Steblov, G., Vasilenko, N., King, R., Prytkov, A., 2006b. Independent
1207 active microplate tectonics of northeast Asia from GPS velocities and block modeling.
1208 Geophys. Res. Lett. 33, 2006GL026077. https://doi.org/10.1029/2006GL026077

1209 Aron, F., Cembrano, J., Astudillo, F., Allmendinger, R.W., Arancibia, G., 2015. Constructing
1210 forearc architecture over megathrust seismic cycles: Geological snapshots from the Maule
1211 earthquake region, Chile. GSA Bulletin 127, 464–479. https://doi.org/10.1130/B31125.1
1212 Audet, P., Bürgmann, R., 2011. Dominant role of tectonic inheritance in supercontinent cycles.
1213 Nature Geoscience 4, 184–187. https://doi.org/10.1038/ngeo1080
1214 Balay, S., Abhyankar, S., Adams, M.F., Benson, S., Brown, J., Brune, P., Buschelman, K.,
1215 Constantinescu, E., Dalcin, L., Dener, A., Eijkhout, V., Gropp, W.D., Hapla, V., Isaac, T.,
1216 Jolivet, P., Karpeev, D., Kaushik, D., Knepley, M.G., Kong, F., Kruger, S., May, D.A.,
1217 McInnes, L.C., Mills, R.T., Mitchell, L., Munson, T., Roman, J.E., Rupp, K., Sanan, P.,
1218 Sarich, J., Smith, B.F., Zampini, S., Zhang, H., Zhang, H., Zhang, J., 2021a. PETSc/TAO
1219 users manual (No. ANL-21/39-Revision 3.16). Argonne National Laboratory.
1220 Balay, S., Abhyankar, S., Adams, M.F., Benson, S., Brown, J., Brune, P., Buschelman, K.,
1221 Constantinescu, E.M., Dalcin, L., Dener, A., Eijkhout, V., Gropp, W.D., Hapla, V., Isaac,
1222 T., Jolivet, P., Karpeev, D., Kaushik, D., Knepley, M.G., Kong, F., Kruger, S., May, D.A.,
1223 McInnes, L.C., Mills, R.T., Mitchell, L., Munson, T., Roman, J.E., Rupp, K., Sanan, P.,
1224 Sarich, J., Smith, B.F., Zampini, S., Zhang, H., Zhang, H., Zhang, J., 2021b. PETSc Web
1225 page [WWW Document]. URL https://petsc.org/
1226 Balay, S., Gropp, W.D., McInnes, L.C., Smith, B.F., 1997. Efficient management of parallelism
1227 in object oriented numerical software libraries, in: Arge, E., Bruaset, A.M., Langtangen,
1228 H.P. (Eds.), Modern Software Tools in Scientific Computing. Birkhäuser Press, pp. 163–
1229 202.
1230 Baldis, B.A., Beresi, M., Bordonaro, O., Vaca, A., 1982. Síntesis evolutiva de la Precordillera
1231 Argentina, in: Actas. Presented at the 5^0 Congreso Latinoamericano de geología, Servicio
1232 Geológico Nacional, Subsecretaría de Minería, Buenos Aires, Argentina, pp. 399–445.
1233 Barber, A.J., 2000. The origin of the Woyla Terranes in Sumatra and the Late Mesozoic
1234 evolution of the Sundaland margin. Journal of Asian Earth Sciences 18, 713–738.
1235 https://doi.org/10.1016/S1367-9120(00)00024-9
1236 Barber, A.J., Crow, M.J., Milsom, J., 2005. Sumatra: Geology, Resources and Tectonic
1237 Evolution. Geological Society of London.
1238 Bevis, M., Kendrick, E., Smalley, R., Brooks, B., Allmendinger, R., Isacks, B., 2001. On the
1239 strength of interplate coupling and the rate of back arc convergence in the central Andes:

1240 An analysis of the interseismic velocity field. Geochemistry, Geophysics, Geosystems 2.
1241 https://doi.org/10.1029/2001GC000198
1242 Bird, P., 2003. An updated digital model of plate boundaries. Geochemistry, Geophysics,
1243 Geosystems 4. https://doi.org/10.1029/2001GC000252
1244 Blacic, J.D., Christie, J.M., 1984. Plasticity and hydrolytic weakening of quartz single crystals.
1245 Journal of Geophysical Research: Solid Earth 89, 4223–4239.
1246 https://doi.org/10.1029/JB089iB06p04223
1247 Blewitt, G., Kreemer, C., Hammond, W.C., Gazeaux, J., 2016. MIDAS robust trend estimator for
1248 accurate GPS station velocities without step detection. Journal of Geophysical Research:
1249 Solid Earth 121, 2054–2068. https://doi.org/10.1002/2015JB012552
1250 Bock, Y., Prawirodirdjo, L., Genrich, J.F., Stevens, C.W., McCaffrey, R., Subarya, C.,
1251 Puntodewo, S.S.O., Calais, E., 2003. Crustal motion in Indonesia from Global Positioning
1252 System measurements. Journal of Geophysical Research: Solid Earth 108.
1253 https://doi.org/10.1029/2001JB000324
1254 Broerse, T., Riva, R., Simons, W., Govers, R., Vermeersen, B., 2015. Postseismic GRACE and
1255 GPS observations indicate a rheology contrast above and below the Sumatra slab. Journal
1256 of Geophysical Research: Solid Earth 120, 5343–5361.
1257 https://doi.org/10.1002/2015JB011951
1258 Brooks, B.A., Bevis, M., Smalley, R., Kendrick, E., Manceda, R., Lauría, E., Maturana, R.,
1259 Araujo, M., 2003. Crustal motion in the Southern Andes (26°–36°S): Do the Andes behave
1260 like a microplate? Geochemistry, Geophysics, Geosystems 4.
1261 https://doi.org/10.1029/2003GC000505
1262 Brooks, B.A., Bevis, M., Whipple, K., Ramon Arrowsmith, J., Foster, J., Zapata, T., Kendrick,
1263 E., Minaya, E., Echalar, A., Blanco, M., Euillades, P., Sandoval, M., Smalley, R.J., 2011.
1264 Orogenic-wedge deformation and potential for great earthquakes in the central Andean
1265 backarc. Nature Geoscience 4, 380–383. https://doi.org/10.1038/ngeo1143
1266 Bürgmann, R., Dresen, G., 2008. Rheology of the Lower Crust and Upper Mantle: Evidence
1267 from Rock Mechanics, Geodesy, and Field Observations. Annual Review of Earth and
1268 Planetary Sciences 36, 531–567. https://doi.org/10.1146/annurev.earth.36.031207.124326

1269 Burov, E.B., Diament, M., 1995. The effective elastic thickness (T e) of continental lithosphere:
1270 What does it really mean? Journal of Geophysical Research: Solid Earth 100, 3905–3927.
1271 https://doi.org/10.1029/94JB02770
1272 Cambiotti, G., 2020. Joint estimate of the coseismic 2011 Tohoku earthquake fault slip and post-
1273 seismic viscoelastic relaxation by GRACE data inversion. Geophysical Journal
1274 International 220, 1012–1022. https://doi.org/10.1093/gji/ggz485
1275 Chlieh, M., Avouac, J.P., Sieh, K., Natawidjaja, D.H., Galetzka, J., 2008. Heterogeneous
1276 coupling of the Sumatran megathrust constrained by geodetic and paleogeodetic
1277 measurements. Journal of Geophysical Research: Solid Earth 113.
1278 https://doi.org/10.1029/2007JB004981
1279 Chlieh, M., De Chabalier, J.B., Ruegg, J.C., Armijo, R., Dmowska, R., Campos, J., Feigl, K.L.,
1280 2004. Crustal deformation and fault slip during the seismic cycle in the North Chile
1281 subduction zone, from GPS and InSAR observations. Geophysical Journal International
1282 158, 695–711. https://doi.org/10.1111/j.1365-246X.2004.02326.x
1283 Chopra, P.N., Paterson, M.S., 1984. The role of water in the deformation of dunite. Journal of
1284 Geophysical Research: Solid Earth 89, 7861–7876.
1285 https://doi.org/10.1029/JB089iB09p07861
1286 Christensen, N.I., 1996. Poisson's ratio and crustal seismology. Journal of Geophysical
1287 Research: Solid Earth 101, 3139–3156. https://doi.org/10.1029/95JB03446
1288 Chulick, G.S., Detweiler, S., Mooney, W.D., 2013. Seismic structure of the crust and uppermost
1289 mantle of South America and surrounding oceanic basins. Journal of South American Earth
1290 Sciences 42, 260–276. https://doi.org/10.1016/j.jsames.2012.06.002
1291 Cisneros, D., Nocquet, J., 2011. Campo de velocidades del Ecuador, obtenido a través de
1292 mediciones de campañes GPS de los ultimos 15 años y medidas de une red GPS
1293 permanente.
1294 Conn, A.R., Gould, N.I.M., Toint, P.L., 2000. Trust Region Methods. SIAM.
1295 Diao, F., Xiong, X., Wang, R., Zheng, Y., Walter, T.R., Weng, H., Li, J., 2014. Overlapping
1296 post-seismic deformation processes: afterslip and viscoelastic relaxation following the
1297 2011 Mw 9.0 Tohoku (Japan) earthquake. Geophys J Int 196, 218–229.
1298 https://doi.org/10.1093/gji/ggt376

1299 Drewes, H., Heidbach, O., 2012a. The 2009 Horizontal Velocity Field for South America and the
1300 Caribbean, in: Kenyon, S., Pacino, M.C., Marti, U. (Eds.), Geodesy for Planet Earth,
1301 International Association of Geodesy Symposia. Springer Berlin Heidelberg, Berlin,
1302 Heidelberg, pp. 657–664. https://doi.org/10.1007/978-3-642-20338-1_81
1303 Drewes, H., Heidbach, O., 2012b. The 2009 Horizontal Velocity Field for South America and
1304 the Caribbean, in: Kenyon, S., Pacino, M.C., Marti, U., Kenyon, S., Pacino, M.C., Marti,
1305 U. (Eds.), Geodesy for Planet Earth. Berlin, Heidelberg, pp. 657–664.
1306 Driscoll, T.A., 2002. Schwarz-Christoffel Mapping, 1st edition. ed. Cambridge University Press,
1307 Cambridge ; New York.
1308 Dziewonski, A.M., Anderson, D.L., 1981. Preliminary reference Earth model. Physics of the
1309 Earth and Planetary Interiors 25, 297–356. https://doi.org/10.1016/0031-9201(81)90046-7
1310 Fitch, T.J., 1972. Plate convergence, transcurrent faults, and internal deformation adjacent to
1311 Southeast Asia and the western Pacific. Journal of Geophysical Research (1896-1977) 77,
1312 4432–4460. https://doi.org/10.1029/JB077i023p04432
1313 Fouedjio, F., Séguret, S., 2016. Predictive Geological Mapping Using Closed-Form Non-
1314 stationary Covariance Functions with Locally Varying Anisotropy: Case Study at El
1315 Teniente Mine (Chile). Nat Resour Res 25, 431–443. https://doi.org/10.1007/s11053-016-
1316 9293-4
1317 Freed, A.M., Hashima, A., Becker, T.W., Okaya, D.A., Sato, H., Hatanaka, Y., 2017. Resolving
1318 depth-dependent subduction zone viscosity and afterslip from postseismic displacements
1319 following the 2011 Tohoku-oki, Japan earthquake. Earth and Planetary Science Letters
1320 459, 279–290. https://doi.org/10.1016/j.epsl.2016.11.040
1321 Fujiwara, T., Kodaira, S., No, T., Kaiho, Y., Takahashi, N., Kaneda, Y., 2011. The 2011
1322 Tohoku-Oki Earthquake: Displacement Reaching the Trench Axis. Science 334, 1240–
1323 1240. https://doi.org/10.1126/science.1211554
1324 Fukuda, J., Johnson, K.M., 2021. Bayesian Inversion for a Stress-Driven Model of Afterslip and
1325 Viscoelastic Relaxation: Method and Application to Postseismic Deformation Following
1326 the 2011 MW 9.0 Tohoku-Oki Earthquake. Journal of Geophysical Research: Solid Earth
1327 126, e2020JB021620. https://doi.org/10.1029/2020JB021620

1328 Furlong, K.P., Govers, R., 1999. Ephemeral crustal thickening at a triple junction:The
1329 Mendocino crustal conveyor. Geology 27, 127–130. https://doi.org/10.1130/0091-
1330 7613(1999)027<0127:ECTAAT>2.3.CO;2
1331 Gabriel, E., Fagg, G.E., Bosilca, G., Angskun, T., Dongarra, J.J., Squyres, J.M., Sahay, V.,
1332 Kambadur, P., Barrett, B., Lumsdaine, A., Castain, R.H., Daniel, D.J., Graham, R.L.,
1333 Woodall, T.S., 2004. Open MPI: Goals, Concept, and Design of a Next Generation MPI
1334 Implementation, in: Kranzlmüller, D., Kacsuk, P., Dongarra, J. (Eds.), Recent Advances in
1335 Parallel Virtual Machine and Message Passing Interface, Lecture Notes in Computer
1336 Science. Springer Berlin Heidelberg, Berlin, Heidelberg, pp. 97–104.
1337 https://doi.org/10.1007/978-3-540-30218-6_19
1338 Gagnon, K., Chadwell, C.D., Norabuena, E., 2005a. Measuring the onset of locking in the Peru–
1339 Chile trench with GPS and acoustic measurements. Nature 434, 205–208.
1340 https://doi.org/10.1038/nature03412
1341 Gagnon, K., Chadwell, C.D., Norabuena, E., 2005b. Measuring the onset of locking in the Peru–
1342 Chile trench with GPS and acoustic measurements. Nature 434, 205–208.
1343 https://doi.org/10.1038/nature03412
1344 Gahalaut, V.K., Jade, S., Catherine, J.K., Gireesh, R., Ananda, M.B., Kumar, P., Narsaiah, M.,
1345 Jafri, S.S.H., Ambikapathy, A., Bansal, A., Chadha, R.K., Gupta, D.C., Nagarajan, B.,
1346 Kumar, S., 2008. GPS measurements of postseismic deformation in the Andaman-Nicobar
1347 region following the giant 2004 Sumatra-Andaman earthquake. Journal of Geophysical
1348 Research: Solid Earth 113. https://doi.org/10.1029/2007JB005511
1349 Genrich, J.F., Bock, Y., McCaffrey, R., Prawirodirdjo, L., Stevens, C.W., Puntodewo, S.S.O.,
1350 Subarya, C., Wdowinski, S., 2000a. Distribution of slip at the northern Sumatran fault
1351 system. J. Geophys. Res. 105, 28327–28341. https://doi.org/10.1029/2000JB900158
1352 Genrich, J.F., Bock, Y., McCaffrey, R., Prawirodirdjo, L., Stevens, C.W., Puntodewo, S.S.O.,
1353 Subarya, C., Wdowinski, S., 2000b. Distribution of slip at the northern Sumatran fault
1354 system. J. Geophys. Res. 105, 28327–28341. https://doi.org/10.1029/2000JB900158
1355 Gerya, T.V., Meilick, F.I., 2011. Geodynamic regimes of subduction under an active margin:
1356 effects of rheological weakening by fluids and melts. Journal of Metamorphic Geology 29,
1357 7–31. https://doi.org/10.1111/j.1525-1314.2010.00904.x

1358 Geuzaine, C., Remacle, J.-F., 2009. Gmsh: A 3-D finite element mesh generator with built-in
1359 pre- and post-processing facilities. International Journal for Numerical Methods in
1360 Engineering 79, 1309–1331. https://doi.org/10.1002/nme.2579
1361 Govers, R., Furlong, K.P., van de Wiel, L., Herman, M.W., Broerse, T., 2018. The Geodetic
1362 Signature of the Earthquake Cycle at Subduction Zones: Model Constraints on the Deep
1363 Processes. Reviews of Geophysics 56, 6–49. https://doi.org/10.1002/2017RG000586
1364 Govers, R., Wortel, M.J.R., 2005. Lithosphere tearing at STEP faults: response to edges of
1365 subduction zones. Earth and Planetary Science Letters 236, 505–523.
1366 https://doi.org/10.1016/j.epsl.2005.03.022
1367 Govers, R., Wortel, M.J.R., 1993. Initiation of asymmetric extension in continental lithosphere.
1368 Tectonophysics 223, 75–96. https://doi.org/10.1016/0040-1951(93)90159-H
1369 Haberland, C., Bohm, M., Asch, G., 2014. Accretionary nature of the crust of Central and East
1370 Java (Indonesia) revealed by local earthquake travel-time tomography. Journal of Asian
1371 Earth Sciences 96, 287–295. https://doi.org/10.1016/j.jseaes.2014.09.019
1372 Hall, R., Clements, B., Smyth, H.R., 2009. Sundaland: Basement Character, Structure and Plate
1373 Tectonic Development. PROCEEDINGS, INDONESIAN PETROLEUM ASSOCIATION
1374 33rd Annual Convention, 2009.
1375 Hall, R., Sevastjanova, I., 2012. Australian crust in Indonesia. Australian Journal of Earth
1376 Sciences 59, 827–844. https://doi.org/10.1080/08120099.2012.692335
1377 Hardebeck, J.L., 2015. Stress orientations in subduction zones and the strength of subduction
1378 megathrust faults. Science 349, 1213–1216. https://doi.org/10.1126/science.aac5625
1379 Hashimoto, C., Noda, A., Sagiya, T., Matsu'ura, M., 2009. Interplate seismogenic zones along
1380 the Kuril–Japan trench inferred from GPS data inversion. Nature Geosci 2, 141–144.
1381 https://doi.org/10.1038/ngeo421
1382 Hayes, G.P., Moore, G.L., Portner, D.E., Hearne, M., Flamme, H., Furtney, M., Smoczyk, G.M.,
1383 2018. Slab2, a comprehensive subduction zone geometry model. Science 362, 58–61.
1384 https://doi.org/10.1126/science.aat4723
1385 Herman, M.W., Govers, R., 2020. Locating Fully Locked Asperities Along the South America
1386 Subduction Megathrust: A New Physical Interseismic Inversion Approach in a Bayesian
1387 Framework. Geochemistry, Geophysics, Geosystems 21, e2020GC009063.
1388 https://doi.org/10.1029/2020GC009063

1389 Hirth, G., Kohlstedt, D.L., 1996. Water in the oceanic upper mantle: implications for rheology,
1390 melt extraction and the evolution of the lithosphere. Earth and Planetary Science Letters
1391 144, 93–108. https://doi.org/10.1016/0012-821X(96)00154-9
1392 Hu, Y., Bürgmann, R., Uchida, N., Banerjee, P., Freymueller, J.T., 2016. Stress-driven relaxation
1393 of heterogeneous upper mantle and time-dependent afterslip following the 2011 Tohoku
1394 earthquake. Journal of Geophysical Research: Solid Earth 121, 385–411.
1395 https://doi.org/10.1002/2015JB012508
1396 Hu, Y., Wang, K., 2012. Spherical-Earth finite element model of short-term postseismic
1397 deformation following the 2004 Sumatra earthquake. Journal of Geophysical Research:
1398 Solid Earth 117. https://doi.org/10.1029/2012JB009153
1399 Hutchison, C.S., 2014. Tectonic evolution of Southeast Asia 60, 18.
1400 Hutchison, C.S., 1994. Gondwana and Cathaysian blocks, Palaeotethys sutures and Cenozoic
1401 tectonics in South-east Asia, in: Giese, P., Behrmann, J. (Eds.), Active Continental
1402 Margins — Present and Past. Springer, Berlin, Heidelberg, pp. 388–405.
1403 https://doi.org/10.1007/978-3-662-38521-0_14
1404 Ikari, M.J., Marone, C., Saffer, D.M., 2011. On the relation between fault strength and frictional
1405 stability. Geology 39, 83–86. https://doi.org/10.1130/G31416.1
1406 Itoh, Y., Nishimura, T., Wang, K., He, J., 2021. New Megathrust Locking Model for the
1407 Southern Kurile Subduction Zone Incorporating Viscoelastic Relaxation and Non-Uniform
1408 Compliance of Upper Plate. Journal of Geophysical Research: Solid Earth 126,
1409 e2020JB019981. https://doi.org/10.1029/2020JB019981
1410 Itoh, Y., Wang, K., Nishimura, T., He, J., 2019. Compliant Volcanic Arc and Backarc Crust in
1411 Southern Kurile Suggested by Interseismic Geodetic Deformation. Geophys. Res. Lett. 46,
1412 11790–11798. https://doi.org/10.1029/2019GL084656
1413 Jin, S., Park, P.-H., 2006a. Strain accumulation in South Korea inferred from GPS
1414 measurements. Earth Planet Sp 58, 529–534. https://doi.org/10.1186/BF03351950
1415 Jin, S., Park, P.-H., 2006b. Strain accumulation in South Korea inferred from GPS
1416 measurements. Earth Planet Sp 58, 529–534. https://doi.org/10.1186/BF03351950
1417 Jin, S., Park, P.-H., Zhu, W., 2007. Micro-plate tectonics and kinematics in Northeast Asia
1418 inferred from a dense set of GPS observations. Earth and Planetary Science Letters 257,
1419 486–496. https://doi.org/10.1016/j.epsl.2007.03.011

1420 Jordan, T.E., Isacks, B.L., Allmendinger, R.W., Brewer, J.A., Ramos, V.A., Ando, C.J., 1983.
1421 Andean tectonics related to geometry of subducted Nazca plate. GSA Bulletin 94, 341–
1422 361. https://doi.org/10.1130/0016-7606(1983)94<341:ATRTGO>2.0.CO;2
1423 Kanamori, H., 1972. Mechanism of tsunami earthquakes. Physics of the Earth and Planetary
1424 Interiors 6, 346–359. https://doi.org/10.1016/0031-9201(72)90058-1
1425 Karig, D.E., 1974. Evolution of Arc Systems in the Western Pacific. Annu. Rev. Earth Planet.
1426 Sci. 2, 51–75. https://doi.org/10.1146/annurev.ea.02.050174.000411
1427 Katsumata, K., Wada, N., Kasahara, M., 2006. Three-dimensional P and S wave velocity
1428 structures beneath the Hokkaido corner, Japan-Kurile arc-arc junction. Earth, Planets and
1429 Space 58, e37–e40. https://doi.org/10.1186/BF03352595
1430 Kawakatsu, H., Kumar, P., Takei, Y., Shinohara, M., Kanazawa, T., Araki, E., Suyehiro, K.,
1431 2009. Seismic Evidence for Sharp Lithosphere-Asthenosphere Boundaries of Oceanic
1432 Plates. Science 324, 499–502. https://doi.org/10.1126/science.1169499
1433 Kellogg, J.N., Vega, V., Stailings, T.C., Aiken, C.L.V., Kellogg, J.N., 1995. Tectonic
1434 development of Panama, Costa Rica, and the Colombian Andes: Constraints from Global
1435 Positioning System geodetic studies and gravity. Geological Society of America Special
1436 Paper 295, 75–90. https://doi.org/10.1130/SPE295-p75
1437 Kendrick, E., Bevis, M., Smalley, R., Brooks, B., 2001. An integrated crustal velocity field for
1438 the central Andes. Geochemistry, Geophysics, Geosystems 2.
1439 https://doi.org/10.1029/2001GC000191
1440 Kendrick, E., Brooks, B.A., Bevis, M., Jr, R.S., Lauria, E., Araujo, M., Parra, H., 2006. Active
1441 orogeny of the south-central Andes studied with GPS geodesy. Revista de la Asociación
1442 Geológica Argentina 61, 555–566.
1443 Khazaradze, G., Klotz, J., 2003. Short- and long-term effects of GPS measured crustal
1444 deformation rates along the south central Andes: SHORT- AND LONG-TERM
1445 DEFORMATION ALONG THE ANDES. J. Geophys. Res. 108.
1446 https://doi.org/10.1029/2002JB001879
1447 Kirby, S.H., 1983. Rheology of the lithosphere. Reviews of Geophysics 21, 1458–1487.
1448 https://doi.org/10.1029/RG021i006p01458
1449 Kita, S., Nakajima, J., Hasegawa, A., Okada, T., Katsumata, K., Asano, Y., Kimura, T., 2014.
1450 Detailed seismic attenuation structure beneath Hokkaido, northeastern Japan: Arc-arc

1451 collision process, arc magmatism, and seismotectonics. Journal of Geophysical Research:
1452 Solid Earth 119, 6486–6511. https://doi.org/10.1002/2014JB011099
1453 Klein, E., Fleitout, L., Vigny, C., Garaud, J.D., 2016. Afterslip and viscoelastic relaxation model
1454 inferred from the large-scale post-seismic deformation following the 2010 Mw 8.8 Maule
1455 earthquake (Chile). Geophysical Journal International 205, 1455–1472.
1456 https://doi.org/10.1093/gji/ggw086
1457 Klein, E., Métois, M., Meneses, G., Vigny, C., Delorme, A., 2018a. Bridging the gap between
1458 North and Central Chile: insight from new GPS data on coupling complexities and the
1459 Andean sliver motion. Geophysical Journal International 213, 1924–1933.
1460 https://doi.org/10.1093/gji/ggy094
1461 Klein, E., Métois, M., Meneses, G., Vigny, C., Delorme, A., 2018b. Bridging the gap between
1462 North and Central Chile: insight from new GPS data on coupling complexities and the
1463 Andean sliver motion. Geophysical Journal International 213, 1924–1933.
1464 https://doi.org/10.1093/gji/ggy094
1465 Klotz, J., Khazaradze, G., Angermann, D., Reigber, C., Perdomo, R., Cifuentes, O., 2001.
1466 Earthquake cycle dominates contemporary crustal deformation in Central and Southern
1467 Andes. Earth and Planetary Science Letters 193, 437–446. https://doi.org/10.1016/S0012-
1468 821X(01)00532-5
1469 Koulali, A., McClusky, S., Susilo, S., Leonard, Y., Cummins, P., Tregoning, P., Meilano, I.,
1470 Efendi, J., Wijanarto, A.B., 2017. The kinematics of crustal deformation in Java from GPS
1471 observations: Implications for fault slip partitioning. Earth and Planetary Science Letters
1472 458, 69–79. https://doi.org/10.1016/j.epsl.2016.10.039
1473 Kreemer, C., Blewitt, G., Klein, E.C., 2014. A geodetic plate motion and Global Strain Rate
1474 Model. Geochemistry, Geophysics, Geosystems 15, 3849–3889.
1475 https://doi.org/10.1002/2014GC005407
1476 Kumar, P., Kawakatsu, H., 2011. Imaging the seismic lithosphere-asthenosphere boundary of the
1477 oceanic plate. Geochemistry, Geophysics, Geosystems 12.
1478 https://doi.org/10.1029/2010GC003358
1479 Li, S., Bedford, J., Moreno, M., Barnhart, W.D., Rosenau, M., Oncken, O., 2018. Spatiotemporal
1480 Variation of Mantle Viscosity and the Presence of Cratonic Mantle Inferred From 8 Years

1481 of Postseismic Deformation Following the 2010 Maule, Chile, Earthquake. Geochemistry,
1482 Geophysics, Geosystems 19, 3272–3285. https://doi.org/10.1029/2018GC007645
1483 Li, S., Fukuda, J., Oncken, O., 2020. Geodetic Evidence of Time-Dependent Viscoelastic
1484 Interseismic Deformation Driven by Megathrust Locking in the Southwest Japan
1485 Subduction Zone. Geophysical Research Letters 47.
1486 https://doi.org/10.1029/2019GL085551
1487 Li, S., Moreno, M., Bedford, J., Rosenau, M., Oncken, O., 2015. Revisiting viscoelastic effects
1488 on interseismic deformation and locking degree: A case study of the Peru-North Chile
1489 subduction zone. Journal of Geophysical Research: Solid Earth 120, 4522–4538.
1490 https://doi.org/10.1002/2015JB011903
1491 Liu, X., Zhao, D., Li, S., 2013. Seismic heterogeneity and anisotropy of the southern Kuril arc:
1492 insight into megathrust earthquakes. Geophysical Journal International 194, 1069–1090.
1493 https://doi.org/10.1093/gji/ggt150
1494 Liu, Z., Owen, S., Dong, D., Lundgren, P., Webb, F., Hetland, E., Simons, M., 2010a. Estimation
1495 of interplate coupling in the Nankai trough, Japan using GPS data from 1996 to 2006. GJI
1496 181, 1313–1328. https://doi.org/10.1111/j.1365-246X.2010.04600.x
1497 Liu, Z., Owen, S., Dong, D., Lundgren, P., Webb, F., Hetland, E., Simons, M., 2010b.
1498 Estimation of interplate coupling in the Nankai trough, Japan using GPS data from 1996 to
1499 2006. GJI 181, 1313–1328. https://doi.org/10.1111/j.1365-246X.2010.04600.x
1500 Loveless, J.P., Meade, B.J., 2011. Spatial correlation of interseismic coupling and coseismic
1501 rupture extent of the 2011 MW = 9.0 Tohoku-oki earthquake. Geophysical Research
1502 Letters 38. https://doi.org/10.1029/2011GL048561
1503 Loveless, J.P., Meade, B.J., 2010. Geodetic imaging of plate motions, slip rates, and partitioning
1504 of deformation in Japan. J. Geophys. Res. 115, B02410.
1505 https://doi.org/10.1029/2008JB006248
1506 Machuca-Mory, D.F., Deutsch, C.V., 2013. Non-stationary Geostatistical Modeling Based on
1507 Distance Weighted Statistics and Distributions. Math Geosci 45, 31–48.
1508 https://doi.org/10.1007/s11004-012-9428-z
1509 Mainprice, D.H., Paterson, M.S., 1984. Experimental studies of the role of water in the plasticity
1510 of quartzites. Journal of Geophysical Research: Solid Earth 89, 4257–4269.
1511 https://doi.org/10.1029/JB089iB06p04257

MATLAB, 2018. R2018b. The MathWorks Inc., Natick, Massachusetts.

Matsu'ura, M., Sato, T., 1989. A dislocation model for the earthquake cycle at convergent plate boundaries. Geophysical Journal International 96, 23–32. https://doi.org/10.1111/j.1365-246X.1989.tb05247.x

McCaffrey, R., 1996. Estimates of modern arc-parallel strain rates in fore arcs. Geology 24, 27–30. https://doi.org/10.1130/0091-7613(1996)024<0027:EOMAPS>2.3.CO;2

McCaffrey, R., 1992. Oblique plate convergence, slip vectors, and forearc deformation. Journal of Geophysical Research: Solid Earth 97, 8905–8915. https://doi.org/10.1029/92JB00483

McFarland, P.K., Bennett, R.A., Alvarado, P., DeCelles, P.G., 2017. Rapid Geodetic Shortening Across the Eastern Cordillera of NW Argentina Observed by the Puna-Andes GPS Array. Journal of Geophysical Research 24. https://doi.org/10.1002/2017JB014739

McKenzie, K.A., Furlong, K.P., 2021. Isolating non-subduction-driven tectonic processes in Cascadia. Geosci. Lett. 8, 10. https://doi.org/10.1186/s40562-021-00181-z

Melosh, H.J., Raefsky, A., 1983. Anelastic response of the Earth to a dip slip earthquake. Journal of Geophysical Research: Solid Earth 88, 515–526. https://doi.org/10.1029/JB088iB01p00515

Melosh, H.J., Raefsky, A., 1981. A simple and efficient method for introducing faults into finite element computations. Bulletin of the Seismological Society of America 71, 1391–1400. https://doi.org/10.1785/BSSA0710051391

Melosh, H.J., Williams, C.A., 1989. Mechanics of graben formation in crustal rocks: A finite element analysis. Journal of Geophysical Research: Solid Earth 94, 13961–13973. https://doi.org/10.1029/JB094iB10p13961

Meltzner, A.J., Sieh, K., Chiang, H.-W., Shen, C.-C., Suwargadi, B.W., Natawidjaja, D.H., Philibosian, B.E., Briggs, R.W., Galetzka, J., 2010. Coral evidence for earthquake recurrence and an A.D. 1390–1455 cluster at the south end of the 2004 Aceh–Andaman rupture. Journal of Geophysical Research: Solid Earth 115. https://doi.org/10.1029/2010JB007499

Metcalfe, I., 2011. Tectonic framework and Phanerozoic evolution of Sundaland. Gondwana Research, Special Section: The South and East Facades of Sundaland 19, 3–21. https://doi.org/10.1016/j.gr.2010.02.016

1542 Metcalfe, I., 2000. The Bentong–Raub Suture Zone. Journal of Asian Earth Sciences 18, 691–
1543 712. https://doi.org/10.1016/S1367-9120(00)00043-2
1544 Métivier, L., Altamimi, Z., Rouby, H., 2020. Past and present ITRF solutions from geophysical
1545 perspectives. Advances in Space Research 65, 2711–2722.
1546 https://doi.org/10.1016/j.asr.2020.03.031
1547 Métois, M., Socquet, A., Vigny, C., 2012. Interseismic coupling, segmentation and mechanical
1548 behavior of the central Chile subduction zone. Journal of Geophysical Research: Solid
1549 Earth 117. https://doi.org/10.1029/2011JB008736
1550 Métois, M., Socquet, A., Vigny, C., Carrizo, D., Peyrat, S., Delorme, A., Maureira, E., Valderas-
1551 Bermejo, M.-C., Ortega, I., 2013. Revisiting the North Chile seismic gap segmentation
1552 using GPS-derived interseismic coupling. Geophysical Journal International 194, 1283–
1553 1294. https://doi.org/10.1093/gji/ggt183
1554 Métois, M., Vigny, C., Socquet, A., 2016. Interseismic Coupling, Megathrust Earthquakes and
1555 Seismic Swarms Along the Chilean Subduction Zone (38°–18°S). Pure Appl. Geophys.
1556 173, 1431–1449. https://doi.org/10.1007/s00024-016-1280-5
1557 Métois, M., Vigny, C., Socquet, A., Delorme, A., Morvan, S., Ortega, I., Valderas-Bermejo, C.-
1558 M., 2014. GPS-derived interseismic coupling on the subduction and seismic hazards in the
1559 Atacama region, Chile. Geophysical Journal International 196, 644–655.
1560 https://doi.org/10.1093/gji/ggt418
1561 Michel, G.W., Yu, Y.Q., Zhu, S.Y., Reigber, C., Becker, M., Reinhart, E., Simons, W.,
1562 Ambrosius, B., Vigny, C., Chamot-Rooke, N., Le Pichon, X., Morgan, P., Matheussen, S.,
1563 2001. Crustal motion and block behaviour in SE-Asia from GPS measurements. Earth and
1564 Planetary Science Letters 187, 239–244. https://doi.org/10.1016/S0012-821X(01)00298-9
1565 Moore, J.C., Saffer, D., 2001. Updip limit of the seismogenic zone beneath the accretionary
1566 prism of southwest Japan: An effect of diagenetic to low-grade metamorphic processes and
1567 increasing effective stress. Geology 29, 183–186. https://doi.org/10.1130/0091-
1568 7613(2001)029<0183:ULOTSZ>2.0.CO;2
1569 Moreno, M., Rosenau, M., Oncken, O., 2010. 2010 Maule earthquake slip correlates with pre-
1570 seismic locking of Andean subduction zone. Nature 467, 198–202.
1571 https://doi.org/10.1038/nature09349

1572 Mouthereau, F., Watts, A.B., Burov, E., 2013. Structure of orogenic belts controlled by
1573 lithosphere age. Nature Geoscience 6, 785–789. https://doi.org/10.1038/ngeo1902
1574 Muto, J., Moore, J.D.P., Barbot, S., Iinuma, T., Ohta, Y., Iwamori, H., 2019. Coupled afterslip
1575 and transient mantle flow after the 2011 Tohoku earthquake. Science Advances 5,
1576 eaaw1164. https://doi.org/10.1126/sciadv.aaw1164
1577 Nishimura, T., 2011a. Back-arc spreading of the northern Izu–Ogasawara (Bonin) Islands arc
1578 clarified by GPS data. Tectonophysics 512, 60–67.
1579 https://doi.org/10.1016/j.tecto.2011.09.022
1580 Nishimura, T., 2011b. Back-arc spreading of the northern Izu–Ogasawara (Bonin) Islands arc
1581 clarified by GPS data. Tectonophysics 512, 60–67.
1582 https://doi.org/10.1016/j.tecto.2011.09.022
1583 Nocquet, J.-M., Jarrin, P., Vallée, M., Mothes, P.A., Grandin, R., Rolandone, F., Delouis, B.,
1584 Yepes, H., Font, Y., Fuentes, D., Régnier, M., Laurendeau, A., Cisneros, D., Hernandez,
1585 S., Sladen, A., Singaucho, J.-C., Mora, H., Gomez, J., Montes, L., Charvis, P., 2017.
1586 Supercycle at the Ecuadorian subduction zone revealed after the 2016 Pedernales
1587 earthquake. Nature Geoscience 10, 145–149. https://doi.org/10.1038/ngeo2864
1588 Nocquet, J.-M., Villegas-Lanza, J.C., Chlieh, M., Mothes, P.A., Rolandone, F., Jarrin, P.,
1589 Cisneros, D., Alvarado, A., Audin, L., Bondoux, F., Martin, X., Font, Y., Régnier, M.,
1590 Vallée, M., Tran, T., Beauval, C., Maguiña Mendoza, J.M., Martinez, W., Tavera, H.,
1591 Yepes, H., 2014. Motion of continental slivers and creeping subduction in the northern
1592 Andes. Nature Geosci 7, 287–291. https://doi.org/10.1038/ngeo2099
1593 Norabuena, E., Leffler-Griffin, L., Mao, A., Dixon, T., Stein, S., Sacks, I.S., Ocola, L., Ellis, M.,
1594 1998. Space Geodetic Observations of Nazca-South America Convergence Across the
1595 Central Andes. Science 279, 358–362. https://doi.org/10.1126/science.279.5349.358
1596 Nostro, C., Piersanti, A., Antonioli, A., Spada, G., 1999. Spherical versus flat models of
1597 coseismic and postseismic deformations. Journal of Geophysical Research: Solid Earth
1598 104, 13115–13134. https://doi.org/10.1029/1999JB900097
1599 Ohzono, M., Sagiya, T., Hirahara, K., Hashimoto, M., Takeuchi, A., Hoso, Y., Wada, Y., Onoue,
1600 K., Ohya, F., Doke, R., 2011a. Strain accumulation process around the Atotsugawa fault
1601 system in the Niigata-Kobe Tectonic Zone, central Japan: Strain field around the

1602 Atotsugawa fault system. Geophysical Journal International 184, 977–990.
1603 https://doi.org/10.1111/j.1365-246X.2010.04876.x
1604 Ohzono, M., Sagiya, T., Hirahara, K., Hashimoto, M., Takeuchi, A., Hoso, Y., Wada, Y., Onoue,
1605 K., Ohya, F., Doke, R., 2011b. Strain accumulation process around the Atotsugawa fault
1606 system in the Niigata-Kobe Tectonic Zone, central Japan. Geophysical Journal
1607 International 184, 977–990. https://doi.org/10.1111/j.1365-246X.2010.04876.x
1608 Ortiz, A., Zambrano, J.J., 1981. La provincia geológica Precordillera Oriental, in: Actas.
1609 Presented at the 8° Congreso Geológico Argentino, Buenos Aires, Argentina, pp. 59–74.
1610 Pearson, D.M., Kapp, P., DeCelles, P.G., Reiners, P.W., Gehrels, G.E., Ducea, M.N., Pullen, A.,
1611 2013. Influence of pre-Andean crustal structure on Cenozoic thrust belt kinematics and
1612 shortening magnitude: Northwestern Argentina. Geosphere 9, 1766–1782.
1613 https://doi.org/10.1130/GES00923.1
1614 Perarnau, M., Gilbert, H., Alvarado, P., Martino, R., Anderson, M., 2012. Crustal structure of the
1615 Eastern Sierras Pampeanas of Argentina using high frequency local receiver functions.
1616 TECTONOPHYSICS 580, 208–217. https://doi.org/10.1016/j.tecto.2012.09.021
1617 Pérez-Gussinyé, M., Lowry, A.R., Morgan, J.P., Tassara, A., 2008. Effective elastic thickness
1618 variations along the Andean margin and their relationship to subduction geometry.
1619 Geochemistry, Geophysics, Geosystems 9. https://doi.org/10.1029/2007GC001786
1620 Pérez-Gussinyé, M., Lowry, A.R., Watts, A.B., 2007. Effective elastic thickness of South
1621 America and its implications for intracontinental deformation. Geochemistry, Geophysics,
1622 Geosystems 8. https://doi.org/10.1029/2006GC001511
1623 Petit, C., Fournier, M., 2005. Present-day velocity and stress fields of the Amurian Plate from
1624 thin-shell finite-element modelling. Geophysical Journal International 160, 357–369.
1625 https://doi.org/10.1111/j.1365-246X.2004.02486.x
1626 Pollitz, F.F., Brooks, B., Tong, X., Bevis, M.G., Foster, J.H., Bürgmann, R., Smalley, R., Vigny,
1627 C., Socquet, A., Ruegg, J.-C., Campos, J., Barrientos, S., Parra, H., Soto, J.C.B., Cimbaro,
1628 S., Blanco, M., 2011a. Coseismic slip distribution of the February 27, 2010 Mw 8.8 Maule,
1629 Chile earthquake. Geophysical Research Letters 38.
1630 https://doi.org/10.1029/2011GL047065
1631 Pollitz, F.F., Bürgmann, R., Banerjee, P., 2011b. Geodetic slip model of the 2011 M9.0 Tohoku
1632 earthquake. Geophysical Research Letters 38. https://doi.org/10.1029/2011GL048632

1633 Pollitz, F.F., Thatcher, W.R., Hearn, E.H., 2010. The resolution of mantle viscosity using nine
1634 years of GPS measurements following the 1999 M=7.1 Hector Mine, CA, earthquake
1635 (Invited). AGU Fall Meeting Abstracts 51, T51F-02.
1636 Prawirodirdjo, L., Bocl, Y., McCaffrey, R., Genrich, J., Calais, E., Stevens, C., Puntodewo,
1637 S.S.O., Subarya, C., Rais, J., Zwick, P., Fauzi, R.M., 1997. Geodetic observations of
1638 interseismic strain segmentation at the Sumatra Subduction Zone. Geophys. Res. Lett. 24,
1639 2601–2604. https://doi.org/10.1029/97GL52691
1640 Prawirodirdjo, L., McCaffrey, R., Chadwell, C.D., Bock, Y., Subarya, C., 2010. Geodetic
1641 observations of an earthquake cycle at the Sumatra subduction zone: Role of interseismic
1642 strain segmentation. Journal of Geophysical Research: Solid Earth 115.
1643 https://doi.org/10.1029/2008JB006139
1644 Qiu, Q., Moore, J.D.P., Barbot, S., Feng, L., Hill, E.M., 2018. Transient rheology of the
1645 Sumatran mantle wedge revealed by a decade of great earthquakes. Nat Commun 9, 995.
1646 https://doi.org/10.1038/s41467-018-03298-6
1647 Ramos, V.A., 1999. Plate tectonic setting of the Andean Cordillera. Episodes Journal of
1648 International Geoscience 22, 183–190. https://doi.org/10.18814/epiiugs/1999/v22i3/005
1649 Ramos, V.A., 1988. Late Proterozoic-Early Paleozoic of South America -a Collisional History.
1650 Episodes Journal of International Geoscience 11, 168–174.
1651 https://doi.org/10.18814/epiiugs/1988/v11i3/003
1652 Ranalli, G., 1995. Rheology of the earth. Chapman & Hall, London; New York.
1653 Rivas, C., Ortiz, G., Alvarado, P., Podesta, M., Martin, A., 2019. Modern crustal seismicity in
1654 the northern Andean Precordillera, Argentina. Tectonophysics 762, 144–158.
1655 https://doi.org/10.1016/j.tecto.2019.04.019
1656 Ruegg, J.C., Rudloff, A., Vigny, C., Madariaga, R., de Chabalier, J.B., Campos, J., Kausel, E.,
1657 Barrientos, S., Dimitrov, D., 2009. Interseismic strain accumulation measured by GPS in
1658 the seismic gap between Constitución and Concepción in Chile. Physics of the Earth and
1659 Planetary Interiors, Earthquakes in subduction zones: A multidisciplinary approach 175,
1660 78–85. https://doi.org/10.1016/j.pepi.2008.02.015
1661 Sagiya, T., Miyazaki, S., Tada, T., 2000a. Continuous GPS Array and Present-day Crustal
1662 Deformation of Japan. Pure appl. geophys. 2303–2322.

1663 Sagiya, T., Miyazaki, S., Tada, T., 2000b. Continuous GPS Array and Present-day Crustal
1664 Deformation of Japan. Pure appl. geophys. 2303–2322.
1665 Satake, K., 2015. Geological and historical evidence of irregular recurrent earthquakes in Japan.
1666 Philosophical Transactions of the Royal Society A: Mathematical, Physical and
1667 Engineering Sciences 373, 20140375. https://doi.org/10.1098/rsta.2014.0375
1668 Satake, K., 1986. Re-examination of the 1940 Shakotan-oki earthquake and the fault parameters
1669 of the earthquakes along the eastern margin of the Japan Sea. Physics of the Earth and
1670 Planetary Interiors 43, 137–147. https://doi.org/10.1016/0031-9201(86)90081-6
1671 Sato, T., Kosuga, M., Tanaka, K., 1986. AFTERSHOCK DISTRIBUTION OF THE 1983
1672 NIHONKAI-CHUBU (JAPAN SEA) EARTHQUAKE DETERMINED FROM
1673 RELOCATED HYPOCENTERS. Journal of Physics of the Earth 34, 203–223.
1674 https://doi.org/10.4294/jpe1952.34.203
1675 Savage, J.C., 1983. A dislocation model of strain accumulation and release at a subduction zone.
1676 Journal of Geophysical Research: Solid Earth 88, 4984–4996.
1677 https://doi.org/10.1029/JB088iB06p04984
1678 Scholz, C.H., 1998. Earthquakes and friction laws. Nature 391, 37–42.
1679 https://doi.org/10.1038/34097
1680 Sébrier, M., Mercier, J.L., Macharé, J., Bonnot, D., Cabrera, J., Blanc, J.L., 1988. The state of
1681 stress in an overriding plate situated above a flat slab: The Andes of central Peru. Tectonics
1682 7, 895–928. https://doi.org/10.1029/TC007i004p00895
1683 Seemüller, W., Sánchez, L., Seitz, M., Drewes, H., 2010a. The position and velocity solution
1684 SIR10P01 of the IGS Regional Network Associate Analysis Centre for SIRGAS (IGS
1685 RNAAC SIR).
1686 Seemüller, W., Sánchez, L., Seitz, M., Drewes, H., 2010b. The position and velocity solution
1687 SIR10P01 of the IGS Regional Network Associate Analysis Centre for SIRGAS (IGS
1688 RNAAC SIR).
1689 Seno, T., Sakurai, T., Stein, S., 1996. Can the Okhotsk Plate be discriminated from the North
1690 American plate? Journal of Geophysical Research: Solid Earth 101, 11305–11315.
1691 https://doi.org/10.1029/96JB00532
1692 Shestakov, N.V., Gerasimenko, M.D., Takahashi, H., Kasahara, M., Bormotov, V.A., Bykov,
1693 V.G., Kolomiets, A.G., Gerasimov, G.N., Vasilenko, N.F., Prytkov, A.S., Timofeev,

1694 V.Yu., Ardyukov, D.G., Kato, T., 2011a. Present tectonics of the southeast of Russia as
1695 seen from GPS observations: Present tectonics of the southeast of Russia. Geophysical
1696 Journal International 184, 529–540. https://doi.org/10.1111/j.1365-246X.2010.04871.x
1697 Shestakov, N.V., Gerasimenko, M.D., Takahashi, H., Kasahara, M., Bormotov, V.A., Bykov,
1698 V.G., Kolomiets, A.G., Gerasimov, G.N., Vasilenko, N.F., Prytkov, A.S., Timofeev,
1699 V.Yu., Ardyukov, D.G., Kato, T., 2011b. Present tectonics of the southeast of Russia as
1700 seen from GPS observations: Present tectonics of the southeast of Russia. Geophysical
1701 Journal International 184, 529–540. https://doi.org/10.1111/j.1365-246X.2010.04871.x
1702 Shi, F., Li, S., Moreno, M., 2020. Megathrust Locking and Viscous Mantle Flow Induce
1703 Continental Shortening in Central Andes. Pure Appl. Geophys. 177, 2841–2852.
1704 https://doi.org/10.1007/s00024-019-02403-0
1705 Shi, X., Kirby, J., Yu, C., Jiménez-Díaz, A., Zhao, J., 2017. Spatial variations in the effective
1706 elastic thickness of the lithosphere in Southeast Asia. Gondwana Research 42, 49–62.
1707 https://doi.org/10.1016/j.gr.2016.10.005
1708 Sibson, R., 1981. A brief description of natural neighbour interpolation. Interpreting Multivariate
1709 Data.
1710 Simons, M., Minson, S.E., Sladen, A., Ortega, F., Jiang, J., Owen, S.E., Meng, L., Ampuero, J.-
1711 P., Wei, S., Chu, R., Helmberger, D.V., Kanamori, H., Hetland, E., Moore, A.W., Webb,
1712 F.H., 2011. The 2011 Magnitude 9.0 Tohoku-Oki Earthquake: Mosaicking the Megathrust
1713 from Seconds to Centuries. Science 332, 1421–1425.
1714 https://doi.org/10.1126/science.1206731
1715 Simons, W.J.F., Socquet, A., Vigny, C., Ambrosius, B. a. C., Abu, S.H., Promthong, C.,
1716 Subarya, C., Sarsito, D.A., Matheussen, S., Morgan, P., Spakman, W., 2007. A decade of
1717 GPS in Southeast Asia: Resolving Sundaland motion and boundaries. Journal of
1718 Geophysical Research: Solid Earth 112. https://doi.org/10.1029/2005JB003868
1719 Sladen, A., Trevisan, J., 2018. Shallow megathrust earthquake ruptures betrayed by their outer-
1720 trench aftershocks signature. Earth and Planetary Science Letters 483, 105–113.
1721 https://doi.org/10.1016/j.epsl.2017.12.006
1722 Stewart, J., Watts, A.B., 1997. Gravity anomalies and spatial variations of flexural rigidity at
1723 mountain ranges. Journal of Geophysical Research: Solid Earth 102, 5327–5352.
1724 https://doi.org/10.1029/96JB03664

1725 Styron, R., Pagani, M., 2020. The GEM Global Active Faults Database. Earthquake Spectra 36,
1726 160–180. https://doi.org/10.1177/8755293020944182
1727 Sun, T., Wang, K., Iinuma, T., Hino, R., He, J., Fujimoto, H., Kido, M., Osada, Y., Miura, S.,
1728 Ohta, Y., Hu, Y., 2014. Prevalence of viscoelastic relaxation after the 2011 Tohoku-oki
1729 earthquake. Nature 514, 84–87. https://doi.org/10.1038/nature13778
1730 Suwa, Y., Miura, S., Hasegawa, A., Sato, T., Tachibana, K., 2006. Interplate coupling beneath
1731 NE Japan inferred from three-dimensional displacement field. Journal of Geophysical
1732 Research: Solid Earth 111. https://doi.org/10.1029/2004JB003203
1733 Tanaka, A., Yamano, M., Yano, Y., Sasada, M., 2004. Geothermal gradient and heat flow data in
1734 and around Japan (I): Appraisal of heat flow from geothermal gradient data. Earth Planet
1735 Sp 56, 1191–1194. https://doi.org/10.1186/BF03353339
1736 Tanioka, Y., Satake, K., Ruff, L., 1995. Total analysis of the 1993 Hokkaido Nansei-Oki
1737 Earthquake using seismic wave, tsunami, and geodetic data. Geophysical Research Letters
1738 22, 9–12. https://doi.org/10.1029/94GL02787
1739 Tatsumi, Y., Otofuji, Y.-I., Matsuda, T., Nohda, S., 1989. Opening of the Sea of Japan back-arc
1740 basin by asthenospheric injection. Tectonophysics 166, 317–329.
1741 https://doi.org/10.1016/0040-1951(89)90283-7
1742 Tichelaar, B.W., Ruff, L.J., 1993. Depth of seismic coupling along subduction zones. Journal of
1743 Geophysical Research: Solid Earth 98, 2017–2037. https://doi.org/10.1029/92JB02045
1744 Trubienko, O., Fleitout, L., Garaud, J.-D., Vigny, C., 2013. Interpretation of interseismic
1745 deformations and the seismic cycle associated with large subduction earthquakes.
1746 Tectonophysics 589, 126–141. https://doi.org/10.1016/j.tecto.2012.12.027
1747 Ueda, H., Ohtake, M., Sato, H., 2003. Postseismic crustal deformation following the 1993
1748 Hokkaido Nansei-oki earthquake, northern Japan: Evidence for a low-viscosity zone in the
1749 uppermost mantle: POSTSEISMIC CRUSTAL DEFORMATION. J. Geophys. Res. 108.
1750 https://doi.org/10.1029/2002JB002067
1751 van Keken, P.E., Kiefer, B., Peacock, S.M., 2002. High-resolution models of subduction zones:
1752 Implications for mineral dehydration reactions and the transport of water into the deep
1753 mantle. Geochemistry, Geophysics, Geosystems 3, 1 of 20–20 20.
1754 https://doi.org/10.1029/2001GC000256

1755 Van Veen, B.A.D., Vatvani, D., Zijl, F., 2014. Tsunami flood modelling for Aceh & west
1756 Sumatra and its application for an early warning system. Continental Shelf Research,
1757 Numerical Modelling of Tsunamis 79, 46–53. https://doi.org/10.1016/j.csr.2012.08.020
1758 Veloza, G., Styron, R., Taylor, M., Mora, A., 2012. Open-source archive of active faults for
1759 northwest South America. GSAT 22, 4–10. https://doi.org/10.1130/GSAT-G156A.1
1760 Verfürth, R., 1994. A posteriori error estimation and adaptive mesh-refinement techniques.
1761 Journal of Computational and Applied Mathematics 50, 67–83.
1762 https://doi.org/10.1016/0377-0427(94)90290-9
1763 Vigny, C., Simons, W.J.F., Abu, S., Bamphenyu, R., Satirapod, C., Choosakul, N., Subarya, C.,
1764 Socquet, A., Omar, K., Abidin, H.Z., Ambrosius, B. a. C., 2005. Insight into the 2004
1765 Sumatra–Andaman earthquake from GPS measurements in southeast Asia. Nature 436,
1766 201–206. https://doi.org/10.1038/nature03937
1767 Vigny, C., Socquet, A., Peyrat, S., Ruegg, J.-C., Métois, M., Madariaga, R., Morvan, S.,
1768 Lancieri, M., Lacassin, R., Campos, J., Carrizo, D., Bejar-Pizarro, M., Barrientos, S.,
1769 Armijo, R., Aranda, C., Valderas-Bermejo, M.-C., Ortega, I., Bondoux, F., Baize, S.,
1770 Lyon-Caen, H., Pavez, A., Vilotte, J.P., Bevis, M., Brooks, B., Smalley, R., Parra, H.,
1771 Baez, J.-C., Blanco, M., Cimbaro, S., Kendrick, E., 2011. The 2010 Mw 8.8 Maule
1772 Megathrust Earthquake of Central Chile, Monitored by GPS. Science 332, 1417–1421.
1773 https://doi.org/10.1126/science.1204132
1774 Villegas-Lanza, J.C., Chlieh, M., Cavalié, O., Tavera, H., Baby, P., Chire-Chira, J., Nocquet, J.-
1775 M., 2016. Active tectonics of Peru: Heterogeneous interseismic coupling along the Nazca
1776 megathrust, rigid motion of the Peruvian Sliver, and Subandean shortening
1777 accommodation. Journal of Geophysical Research: Solid Earth 121, 7371–7394.
1778 https://doi.org/10.1002/2016JB013080
1779 Wackernagel, H., 2003. Ordinary Kriging, in: Wackernagel, H. (Ed.), Multivariate Geostatistics:
1780 An Introduction with Applications. Springer, Berlin, Heidelberg, pp. 79–88.
1781 https://doi.org/10.1007/978-3-662-05294-5_11
1782 Wada, I., Wang, K., 2009. Common depth of slab-mantle decoupling: Reconciling diversity and
1783 uniformity of subduction zones. Geochemistry, Geophysics, Geosystems 10.
1784 https://doi.org/10.1029/2009GC002570

1785 Wang, K., Hu, Y., Bevis, M., Kendrick, E., Smalley, R., Vargas, R.B., Lauría, E., 2007. Crustal
1786 motion in the zone of the 1960 Chile earthquake: Detangling earthquake-cycle deformation
1787 and forearc-sliver translation: CHILE EARTHQUAKE CRUSTAL MOTION. Geochem.
1788 Geophys. Geosyst. 8. https://doi.org/10.1029/2007GC001721
1789 Wang, K., Hu, Y., He, J., 2012. Deformation cycles of subduction earthquakes in a viscoelastic
1790 Earth. Nature 484, 327–332. https://doi.org/10.1038/nature11032
1791 Wang, M., Li, Q., Wang, F., Zhang, R., Wang, Y., Shi, H., Zhang, P., Shen, Z., 2011. Far-field
1792 coseismic displacements associated with the 2011 Tohoku-oki earthquake in Japan
1793 observed by Global Positioning System. Chin. Sci. Bull. 56, 2419–2424.
1794 https://doi.org/10.1007/s11434-011-4588-7
1795 Wang, Z., Zhao, D., 2005. Seismic imaging of the entire arc of Tohoku and Hokkaido in Japan
1796 using P-wave, S-wave and sP depth-phase data. Physics of the Earth and Planetary
1797 Interiors 152, 144–162. https://doi.org/10.1016/j.pepi.2005.06.010
1798 Watts, A.B., 2015. 6.01 - Crustal and Lithosphere Dynamics: An Introduction and Overview, in:
1799 Schubert, G. (Ed.), Treatise on Geophysics (Second Edition). Elsevier, Oxford, pp. 1–44.
1800 https://doi.org/10.1016/B978-0-444-53802-4.00110-X
1801 Watts, A.B., Lamb, S.H., Fairhead, J.D., Dewey, J.F., 1995. Lithospheric flexure and bending of
1802 the Central Andes. Earth and Planetary Science Letters 134, 9–21.
1803 https://doi.org/10.1016/0012-821X(95)00095-T
1804 Weaver, R., Roberts, A.P., Flecker, R., Macdonald, D.I.M., Fot'yanova, L.M., 2003.
1805 Geodynamic implications of paleomagnetic data from Tertiary sediments in Sakhalin,
1806 Russia (NW Pacific). Journal of Geophysical Research: Solid Earth 108.
1807 https://doi.org/10.1029/2001JB001226
1808 Weiss, J.R., Brooks, B.A., Foster, J.H., Bevis, M., Echalar, A., Caccamise, D., Heck, J.,
1809 Kendrick, E., Ahlgren, K., Raleigh, D., Smalley, R., Vergani, G., 2016. Isolating active
1810 orogenic wedge deformation in the southern Subandes of Bolivia. Journal of Geophysical
1811 Research: Solid Earth 121, 6192–6218. https://doi.org/10.1002/2016JB013145
1812 Wessel, P., Luis, J.F., Uieda, L., Scharroo, R., Wobbe, F., Smith, W.H.F., Tian, D., 2019. The
1813 Generic Mapping Tools Version 6. Geochemistry, Geophysics, Geosystems 20, 5556–
1814 5564. https://doi.org/10.1029/2019GC008515

White, S.M., Trenkamp, R., Kellogg, J.N., 2003. Recent crustal deformation and the earthquake cycle along the Ecuador–Colombia subduction zone. Earth and Planetary Science Letters 216, 231–242. https://doi.org/10.1016/S0012-821X(03)00535-1

Williams, T.B., Kelsey, H.M., Freymueller, J.T., 2006. GPS-derived strain in northwestern California: Termination of the San Andreas fault system and convergence of the Sierra Nevada–Great Valley block contribute to southern Cascadia forearc contraction. Tectonophysics 413, 171–184. https://doi.org/10.1016/j.tecto.2005.10.047

Wimpenny, S., Copley, A., Benavente, C., Aguirre, E., 2018. Extension and Dynamics of the Andes Inferred From the 2016 Parina (Huarichancara) Earthquake. Journal of Geophysical Research: Solid Earth 123, 8198–8228. https://doi.org/10.1029/2018JB015588

Yamagiwa, S., Miyazaki, S., Hirahara, K., Fukahata, Y., 2015. Afterslip and viscoelastic relaxation following the 2011 Tohoku-oki earthquake (M_w 9.0) inferred from inland GPS and seafloor GPS/Acoustic data. Geophys. Res. Lett. 42, 66–73. https://doi.org/10.1002/2014GL061735

Yoshioka, S., 2013. Interplate coupling along the Nankai Trough, southwest Japan, inferred from inversion analyses of GPS data: Effects of subducting plate geometry and spacing of hypothetical ocean-bottom GPS stations 10.

Yoshioka, S., Matsuoka, Y., 2013. Interplate coupling along the Nankai Trough, southwest Japan, inferred from inversion analyses of GPS data: Effects of subducting plate geometry and spacing of hypothetical ocean-bottom GPS stations. Tectonophysics, Great Earthquakes along Subduction Zones 600, 165–174. https://doi.org/10.1016/j.tecto.2013.01.023